In-vivo Raman spectroscopy: from basics to applications

Eliana Cordero
Ines Latka
Christian Matthäus
Iwan W. Schie
Jürgen Popp

SPIE.

In-vivo Raman spectroscopy: from basics to applications

Eliana Cordero,[a,†] Ines Latka,[a,†] Christian Matthäus,[a,b] Iwan W. Schie,[a,*] and Jürgen Popp[a,b]

[a]Leibniz Institute of Photonic Technology, Albert-Einstein-Straße 9, Jena, Germany
[b]Friedrich Schiller University Jena, Institute of Physical Chemistry and Abbe Center of Photonics, Jena, Germany

Abstract. For more than two decades, Raman spectroscopy has found widespread use in biological and medical applications. The instrumentation and the statistical evaluation procedures have matured, enabling the lengthy transition from *ex-vivo* demonstration to *in-vivo* examinations. This transition goes hand-in-hand with many technological developments and tightly bound requirements for a successful implementation in a clinical environment, which are often difficult to assess for novice scientists in the field. This review outlines the required instrumentation and instrumentation parameters, designs, and developments of fiber optic probes for the *in-vivo* applications in a clinical setting. It aims at providing an overview of contemporary technology and clinical trials and attempts to identify future developments necessary to bring the emerging technology to the clinical end users. A comprehensive overview of *in-vivo* applications of fiber optic Raman probes to characterize different tissue and disease types is also given. © The Authors. Published by SPIE under a Creative Commons Attribution 3.0 Unported License. Distribution or reproduction of this work in whole or in part requires full attribution of the original publication, including its DOI. [DOI: 10.1117/1.JBO.23.7.071210]

1 Introduction

Raman spectroscopy is a label-free, nondestructive, and non-invasive method that provides information about the molecular composition and structure of a sample. It has found widespread use in the fields of material sciences, pharmaceutical analysis, inline and offline process controlling, airport security, and many others. In the last few decades, Raman spectroscopy has also begun to emerge as a promising tool for biomedical analytics and clinical diagnostics, such as the detection and staging of cancer, and has been validated in countless *ex-vivo* studies.[1–11] Due to the highly promising results, there has been an incredible effort to move Raman spectroscopy to clinical *in-vivo* applications, where the method can unfold its full diagnostic potential. Although these *in-vivo* studies demonstrate a superb diagnostic potential of Raman spectroscopy in clinical surroundings, they also reveal technological challenges and shortcomings of the method. Due to the highly complex implementation of the technique for *in-vivo* applications it is often difficult, especially for novice scientists in the field of *in-vivo* Raman spectroscopy, to assess the relevant instrumentational design parameters and their influence on the detected signal, the different available fiber optical Raman probe designs, and the readily evaluated *in-vivo* applications.

The implementation of Raman spectroscopy for clinical applications significantly differs from Raman-based analysis of prokaryotic and eukaryotic cells. For example, to provide easy access to most anatomical locations *in-vivo*, fiber optic Raman probes, which are designed for specific applications and are available in a large number of configurations, are required. Due to the generation of a strong Raman background in the fiber, the development of those probes is highly complex and complicates the development of single-use probes. Moreover, probes have to be designed in a way that allows sustainable sterilization procedures to be routinely used in a medical environment. Because fiber optic Raman probes are usually single-point sensors, efforts have to be made to register the measurement spot at the body site to determine the precise location of the optical biopsy. This is often achieved through image guidance, and the combination with other modalities, such as white-light or fluorescence imaging, optical coherence tomography (OCT), optoacoustic or magnetic resonance (MR) tomography, and many others. The additional imaging modalities can also deliver complementary information of the target region and can significantly boost sensitivity and specificity. It is well-known that in biomedical applications intrinsic autofluorescence can easily obscure the weak Raman signal.[12] This can, for the most part, be circumvented using 785 or 830 nm as the excitation wavelength and often in combination with other software[13] or hardware-based methods,[14] such as time gating,[15] frequency modulation,[16] and shifted excitation.[17,18]

In addition to the Raman probes, the entire Raman system, including the narrowband laser source, the optical and electronic components, the software for the device controlling, and data processing are underlying stringent requirements to achieve desirable results. Moreover, the Raman device has to be developed in agreement with local and global medical regulatory standards for the application in clinical studies. This includes risk analysis, which has to prove that the benefits provided by the method outweigh possible risks. An ongoing problem in the field is also the frequently observed inconsistencies of spectral biomarkers for the same diseases. When proper spectral

*Address all correspondence to: Iwan W. Schie, E-mail: iwan.schie@leibniz-ipht.de

†Equally contributing authors

disease markers are available, real-time analysis of the measured Raman spectra is a key requirement for clinical applications. This normally requires a sophisticated statistical analysis,[19–21] relying on pre-established databases with a multitude of stored sample data.

This review aims to provide an overview of the different aspects and challenges for moving Raman spectroscopy from research laboratories to clinics to novice scientists in the field of *in-vivo* Raman spectroscopy. The overview starts with the basic requirements for the instrumentation and outlines the relevant instrumentational parameters, which are needed to reliably detect the weak Raman signal, following an outline of common fiber optic Raman probe developments and common geometries for *in-vivo* applications. Finally, the review provides a comprehensive summary focusing specifically on *in-vivo* applications, using Raman spectroscopy of different disease types and different organs.

2   Raman Instrumentation

The successful implementation of any application using Raman spectroscopy is tightly bound by the instrumentational parameters, which have to be chosen very carefully to measure the weak Raman signals often in the presence of a high background. As such, this section outlines the most important factors for the required components, such as excitation sources, detectors, and spectrometers, and relates the information to the relevant parameters, such as linewidth, noise sources, and resolution. A comprehensive overview of all discussed parameters is summarized in Table 1.

In comparison with most eukaryotic and prokaryotic cells, the Raman signals of histopathological tissue biopsies and *in-vivo* measurements are highly prone to exhibit a strong autofluorescence. While other methods such as fluorescence lifetime microscopy (FLIM) rely on the presence of tissue auto-fluorescence, in Raman spectroscopy the presence of fluorescence creates significant complications. To overcome these drawbacks, near-infrared lasers, most commonly 785 and 830 nm, are used for the excitation of a Raman signal from tissue samples. Due to the narrow spectral width of vibrational bands, which are on the order of a few cm^{-1}, the linewidth for the excitation lasers is constrained, which means that the excitation linewidth should be <0.1 nm to achieve high-resolution spectra. Most of the excitation sources used for biomedical Raman spectroscopy exhibit linewidths of a few picometers with a high excitation power, resulting in higher cost. For low-cost implementations it is, therefore, worthwhile to consider the appropriate laser parameters.

For imaging applications on *ex-vivo* biopsies, the sample is usually placed on an $x - y$ translational stage with submicrometer step-size resolution and illuminated using an objective lens with a high numerical aperture (NA), typically >NA 0.5 and most commonly close to NA 1.0. This is further combined with appropriate illumination and collection optics, which ensure a signal generation and collection from a diffraction-limited spot. When the proper aperture is added in the conjugate focal plane, the Raman acquisition can be operated confocally and enables a three-dimensional (3-D) sectioning of the biopsy sample. Using a confocal Raman implementation, a biopsy probe can be easily mapped, and the biochemical information can be directly correlated to the histopathological hematoxylin and eosin (H&E) staining. A typical Raman imaging setup is shown in Fig. 1(a) and two exemplary Raman spectra of lipid-rich and protein-rich tissue are shown in Fig. 1(b). A comprehensive overview of different Raman-instrumentation schemes, which can be combined with the various probe designs, is given in Refs. 2 and 22.

Table 1 These device parameters are most commonly found in clinical *in-vivo* Raman spectroscopy. The table provides only a general overview of the available parameter space. In some implementations, the parameters can vary from the parameters in the table. Moreover, keep in mind that many of the parameters are coupled.

| Device	Relevant parameters	Typical parameter values	Influences
Detector	QE	30 to 90% @ 900 nm	SNR, acquisition time
	Read-out-speed	16 kHz to 8 MHz	SNR; number of frames/s
	Read noise	3 to 20 e − /pixel	SNR; acquisition time
	Dark current	0.0001 to 0.03 e − /s/pixel @ at −80°C	SNR; acquisition time
	Number of pixels	Horizontally: 532 to 2048	Spectral range
	Pixel size	Vertically: 100 to 2048	Etendue
		$13 \times 13\ \mu m^2$ to $26 \times 26\ \mu m^2$	Resolution
Excitation sources	Wavelengths	785 nm; 830 nm; 1064 nm	Autofluorescence; SNR
	Spectral linewidth	typ. <100 pm	Resolution
	Excitation power	10 to 150 mW	SNR; sample damage
Spectrometer	$f/\#$	1.8 to 9.7	Light gathering ability
	Slit width	50 to 200 μm	Resolution
	Focal length	150 to 750 μm	Resolution
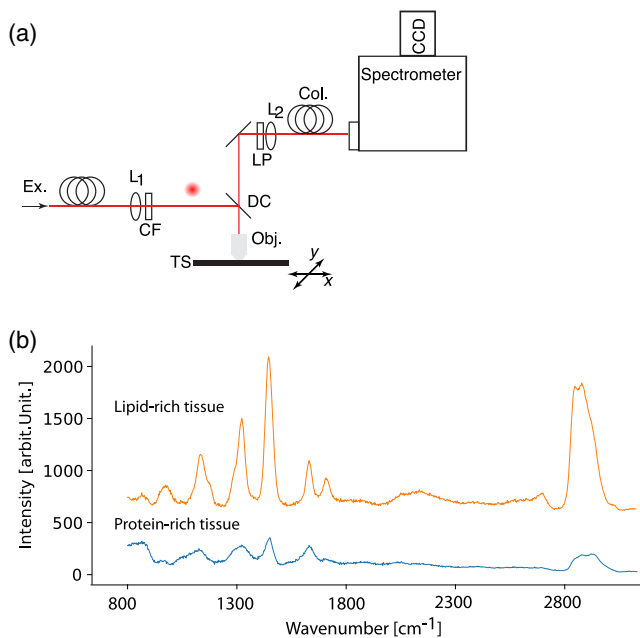
Fig. 1 (a) Typical Raman setup for the acquisition of Raman images of biopsies. Required components are L1-2-fiber coupling lens, CL, cleanup filter; DC, dichroic filter; LP, longpass filter; Obj., objective lens; collection and illumination fiber; and TS, translational stage; (b) typical Raman spectra from lipid- and protein-rich areas of a tissue sample.

Due to long acquisition times, typically on the order of seconds for a single spectrum, Raman imaging is usually not an option for *in-vivo* applications. *In-vivo* measurements are, therefore, most commonly performed by acquiring single-point Raman spectra using fiber optic probes. The design of such Raman probes will be discussed in detail in Sec. 3 of this review.

The key component of a Raman system is the detector, which in most cases is a charged coupled device (CCD). Several important factors have to be considered when choosing the appropriate CCD array for any Raman spectroscopy application. Specifically, the noise level and the quantum efficiency are of great importance. Because of the very low intensity of a Raman signal, typically on the order of 10^4 to 10^5 collected photons for an entire Raman spectrum from a protein-rich tissue sample, using a 785-nm excitation with an excitation of about 50-mW power in the sample plane, a collection NA of 0.35, and 100-μm spot size, it is crucial that the quantum efficiency is high. Keeping in mind that while 10^5 photons are quite a large number in comparison with many other applications, the total number of photons is typically distributed over 600 CCD-pixels, which results on average in <170 photons per pixel. For high-performance scientific CCD cameras that are currently commercially available, the QE is above 90% for the low-wavenumber region, which is between 800 and 910 nm, corresponding to 238 and 1750 cm^{-1}, respectively, for a 785-nm excitation laser. This allows the photons generated in the low-wavenumber region to be efficiently detected. For the high-wavenumber region, which is located between 1006 and 1030 nm for a 785-nm excitation laser, corresponding to 2800 and 3000 cm^{-1}, respectively, the QE is significantly reduced due to the band gap of silica. The OH stretching region of water, which extends all the way to 3800 cm^{-1}, corresponding to 1120 nm, exhibits an even lower QE, i.e., <10%. Generally, photons are not detectable

above 1100 nm using silicon-based CCD detectors. This is of interest because it has been previously demonstrated that the water region can provide valuable information in differentiating tumor from nontumor tissue.[23]

There are several different architecture-types of CCDs available, e.g., front-illuminated (FI), back-illuminated (BI), and back-illuminated deep-depletion (BI-DD) cameras. FI cameras have QEs well below 50% for the wavelength regions mentioned above and are only suitable for applications where this lack of QE can be compensated for by the excitation power or acquisition time. However, FI cameras are also available at a lower price, compared with the two other designs, and have nearly no dark current. The BI-CCD cameras have significantly higher QE than FI-CCD cameras but can suffer from etaloning, which is specifically disruptive when dealing with high fluorescence backgrounds. Etaloning is created by NIR photons that were not absorbed in the photosensitive region but reflected at the detector interface, creating a ringing pattern on the spectrum and significantly altering the Raman spectrum. BI-DD-CCD cameras have a thicker photosensitive region, which helps to reduce the etaloning effect and provides the highest QE in the NIR region, but it also comes at a higher cost.

There have been new developments toward the implementation of InGaAs detectors for the short-wave infrared (SWIR) region. Although some promising first results have been demonstrated by the group around Puppels,[24] one of the main problems is the significantly higher dark noise and read noise, which can be quite challenging for some applications. Moreover, due to the $1/\lambda^4$ dependency of the Raman intensity on the excitation wavelength λ, the Raman signal generation for a 1064-nm excitation is reduced 3.4-fold in comparison with a 785-nm excitation.

There are two main noise sources for the signal acquisition using CCD cameras: read noise and dark noise. As the name suggests, read noise is generated during the read-out process of the charges from the chip and the preamplification step on the CCD camera. In addition to the device-associated noise sources, for most applications the fundamental limit for the recovery of a Raman signal is the photon shot noise. Read noise depends on the acquisition speed and varies for commonly used scientific CCD detectors between 3 and 20 electrons per pixel for comparable models from different manufacturers. Hence, specifically for low-signal applications, it is important to ensure that the right acquisition speed is chosen to ensure the highest achievable signal-to-noise ratio (SNR). Electron multiplying CCDs (EMCCDs) are frequently mentioned and have readily been used in Raman spectroscopy of biological samples. These, however, only help to circumvent the read noise using electron amplification before the electron-to-voltage conversion in the AD unit. An often-unmentioned fact about EMCCDs is that they have a higher charge transfer noise, which is given by a factor of $\sqrt{2}$. This means that only for acquisition at a very low-signal level, i.e., 10 to 20 photons per pixel, does the EMCCD outperform a CCD. However, due to the higher noise factor for longer acquisition times and higher photon levels, which is the most common case for Raman spectroscopy, the noise level of an EMCCD will be higher than for a CCD. Also, the cost for an EMCCD detector is significantly higher than any of the standard CCD detectors. A good comparison for the noise performance of different detectors is given in Ref. 25. To measure the read noise of a CCD detector, one can simply acquire a dark spectrum at a short

acquisition time, e.g., 50 ms, and very small number of vertical pixels, ensuring that the dark current becomes negligible. When no specific imaging information is required, it is possible to perform a vertical hardware binning of the entire CCD-chip or a defined region. This can help to increase the signal and ensures that read noise is only affecting individual pixels. However, for some implementations, such as line-excitation or spatial-offset Raman spectroscopy (SORS), it is important to retain the vertical information on the detector because it is correlated to spatial information in the sample. Here, the SNR level is reduced in comparison with comparable measurements with full vertical binning.

In addition to the read noise, dark noise is an important factor to consider when choosing the right CCD detector for biomedical Raman applications. Dark noise occurs from thermally generated electrons in the silicon structure of the CCD and is highly temperature dependent. Hence, all common detectors in Raman spectroscopy are cooled. Nowadays, thermoelectric cooling is the method of choice, whereas liquid-nitrogen-cooled detectors are found less frequently in laboratories. The large and cumbersome liquid-nitrogen-cooled detectors would also further complicate the transition of Raman devices to clinics, where space in the operating theater is very limited. Typical values for the dark current at −80°C vary between 0.0001 and 0.03 electrons per second per pixel, with significantly lower values for FI-CCDs than for BI-DD-CCDs. The generation of dark noise has also to be considered for any Raman spectroscopy application. For short acquisition times, i.e., <1 s, and a vertical binning of a few dozen of pixels, the dark noise contribution is negligible and way below the read noise level. If, however, the signal acquisition is on the order of a few seconds, or a large number of pixels are vertically binned, which is common when using Raman fiber probes with multiple collection fibers, it can become the limiting factor. Considering typical fiber probes with 10 collection fibers, with a core diameter of 200 μm, an imaging ratio, which is the magnification of the entrance slit into the detection plane, of the spectrometer of one, and a pixel size of 20 μm, a total of 100 pixels will be illuminated. Performing a vertical binning over 100 pixels and an acquisition time of 10 s, the dark current for typical BB-DD CCDs is readily 30 electrons per second per pixel, resulting in a dark noise of 5.4 electrons per pixel, which is higher than the read noise for some available detectors. Nevertheless, for most *in-vivo* and *ex-vivo* Raman applications, the main noise factor stems from shot noise of the fluorescence signal, as fluorescence can seldom be completely avoided. Shot noise is the random statistical fluctuation of the arrival time of photons at the detector, and it follows a Poisson distribution. The fluctuation in the number of arrived photons is described by $\sqrt{N}$, where N is the number of photons. For Raman spectroscopy, this specifically means that if the fluorescence signal is large, the random fluctuation in the photon arrival can be just as high or higher as the measured Raman signal, which places a fundamental limit on the Raman signal detection. For example, when 20 Raman photons arrive on a single detector pixel and the number of fluorescence photons at the same pixel is 400, the SNR just due to shot noise is already 1, in combination with the other noise sources, the SNR will be <1. For any meaningful classification, an SNR > 5 is usually required.

The generated Raman signal is dispersed onto the CCD detector through a spectrometer. There are several types of spectrometers that are employed for Raman spectroscopy, such as lens-based and Czerny–Turner arrangements, each having specific advantages and disadvantages. There are a few factors that have to be considered when choosing the right spectrometer, such as spectral resolution, light-collection ability, the diffraction efficiency, imaging artifacts, and scattering suppression. Many of those parameters are closely interconnected. The most obvious parameter for a spectrometer is the achievable spectral resolution. The resolution depends primarily on the focal length, which is the focal length of the mirror or lens, slit-width, groove density of the diffraction grating, and the detector pixel dimension. In most Raman fiber probe schemes, the linearly arranged collection fibers act as the entrance slit and define the aperture size. In general, it is desirable to detect the entire spectral region between ∼300 and 3800 cm^{-1} at once, which puts a constraint on the usable grating and the achievable spectral resolution, considering a fixed sensor size. There are implementations that allow imaging the low-wavenumber and high-wavenumber regions, vertically offset on the same detector, enabling measurement of the full spectral range at increased resolution. The desired spectral resolution also constrains the focal length and the light-collection ability of a spectrometer, i.e., the higher the resolution, the longer the spectrometer and the lower the light-collection ability. The typical f-numbers ($f/\#$), which is the system's focal length to the entrance aperture ratio, range between $f/1.8$ and $f/6.5$ for typical Raman spectrometers, where the lower number means a higher light-collection ability. Please keep in mind that if a fiber is used to couple the light to the spectrometer, the fiber has to match the $f/\#$ to ensure optimal coupling and best imaging performance of the spectrometer. Another factor to consider when using a spectrometer is the imaging performance, which is explicitly important when working with Raman fiber probes with multiple collection fibers that are imaged on the CCD detector. For example, most Czerny–Turner spectrometer designs can exhibit strong astigmatism, which leads to the so-called bowtie effect when using fibers. Here, only the center wavelength is properly imaged onto the detector while wavelengths further away from the central wavelength experience a vertical spreading. This becomes a significant problem when using fibers arranged vertically in a line because the signals from the individual fibers start bleeding into the neighboring ones. Lens-based spectrometers exhibit excellent imaging properties with nearly no bowtie effect, but they have, on the other hand, a significant problem with out-of-plane diffraction, which is caused by the diffraction grating and rays vertically offset to the optical axis. This results in a curvature of the input from an input fiber-line array.[26] There are, however, computational options to correct for those artifacts.[27] Recently, new commercially available spectrometers that offer superb imaging properties with little aberration have been launched.

3 Fiber and Probe Development

The key component for moving Raman spectroscopy to clinical *in-vivo* applications is fiber optical Raman probes. Over the years, a large literature body has emerged on the different types of Raman probe configurations, often too large to be assessed by a novice scientist. Each specific probe configuration can lead to different types of information, resulting in a differentiated interpretation of the data. Moreover, the number of available probe designs is constantly increasing because new probes not only are designed to perform Raman spectroscopy but also include other optical modalities, such as

autofluorescence, OCT, reflectance, just to name a few. As such, it is paramount to understand the different probe designs, how they differ, and what type of information they can provide. In this article, we give a detailed overview of different probe configurations and provide information on the possible applications.

Optical fiber sensors are increasingly used in health monitoring devices. The characteristic features of silica optical fibers, i.e., small diameter, user-defined length, and high mechanical flexibility, allow facilitating the positioning of the sensor head at remote or otherwise difficult-to-access (body) sites. This permits the development of Raman probes that can fit in the instrument channel of standard medical endoscopes, and the insensitivity of optical fibers to electromagnetic fields enables applications in combination with magnetic resonance imaging (MRI). Additionally, fiber-based sensors do not interfere with conventional electronics, are nontoxic and chemically inert, and enable Raman spectroscopy to access hard-to-reach locations *in vivo*. The implementation of such optical Raman fiber probes can be quite complex. For example, the intensity of the Raman signal generated along the length of silica-based optical fibers can overshadow the generated Raman signal from the sample. Therefore, excitation and detection paths are usually separated into individual fibers to apply appropriate filtering at the distal fiber ends. The excitation fiber is supplemented with a narrowband or a shortpass filter to suppress the silica-based Raman background. In the collection path, on the other hand, a longpass filter is needed to prevent reflected or backscattered laser light from re-entering the fiber. Oftentimes, a multitude of collection fibers is used to improve collection efficiency. At the proximal end, the collection fibers are aligned to efficiently couple the detected Raman signal into the spectrometer. Huang et al.[28] designed a special round-to-parabolic fiber bundle comprising 64 fibers (100-μm-core diameter, NA, 0.22) packed in a round geometry at the collection end but spread out into a parabolic linear array in an orientation opposite to the image aberration of the lens-based spectrograph at the spectrograph's entrance site.

In addition to standard optical fibers, there are a variety of optical fibers types that have also been employed, e.g., hollow,[29] microstructured,[30] bandgap,[31] or multicore[32] fibers. However, the development in recent years shows that, due to easy availability and low cost, mostly standard silica fibers are used. An overview of basic Raman fiber probe designs is given in Ref. 33. Here, the focus will be on fiber optic Raman probes used or intended for *in-vivo* applications.

The Raman fiber probe design is strongly dependent on the application. It is obvious that different constraints exist when using the Raman probe, e.g., within a cardiovascular catheter as compared with measurements in the oral cavity or on the skin. Therefore, not only are spectroscopic parameters, such as the design of the filters, the collection efficiency, and the beam steering properties, important, but first and foremost, the probe diameter and flexibility of the probe have to be considered. Of course, size restrictions are less limiting for skin applications in comparison with cardiovascular applications. Additionally, for applications in hospitals, the designs of fiber optic probes have to conform to hospital guidelines, i.e., the entire fiber-spectroscopic system has to be enclosed to avoid stray light and fit on a small transportable cart for the operating theater. The clearance for the European market requires CE certification. With this marking, the manufacturer or importer declares

compliance with the relevant EU legislation applicable to a product, regardless of where it was manufactured. Concerning the laser powers at the sample position, the guidelines are defined by ANSI Standard Z136.3–2011 "Safe Use of Lasers in Health Care" for the U.S. and EN 60825-1/A2 for Europe. Because of performing *in-vivo* experiments in patients, biocompatible materials should be used to avoid toxic effects.[34] Furthermore, the optical fiber probe has to withstand hospital sterilization procedures.[1]

3.1 Basic Raman Probe Setups

One major difference between endoscopic Raman probes is whether they are confocal or volume probes. For illustration purposes, Fig. 2(a) shows an endoscopic volume probe, also known as a nonsuperficial or nonconfocal probe. These are endoscopic probes without any focusing optics and are the simplest endoscopic fiber optical Raman probes. Figure 2(b) shows a confocal endoscopic fiber optical Raman probe, which is more complex than the nonconfocal probe due to the addition of extra optical components, such as ball lens, gradient index lens (GRIN lens),[35] or aspheric lenses.[36] To allow for side-viewing application, mirrors [Fig. 2(c)], or prisms can be added. One possible confocal handheld Raman probe design described in Ref. 37 is shown in Fig. 2(d). The handheld Raman probe comprises two optical arms: one for the delivery of the excitation light, the other for the collection of the Raman scattered signal, integrated with optical filtering modules. The excitation light is focused on
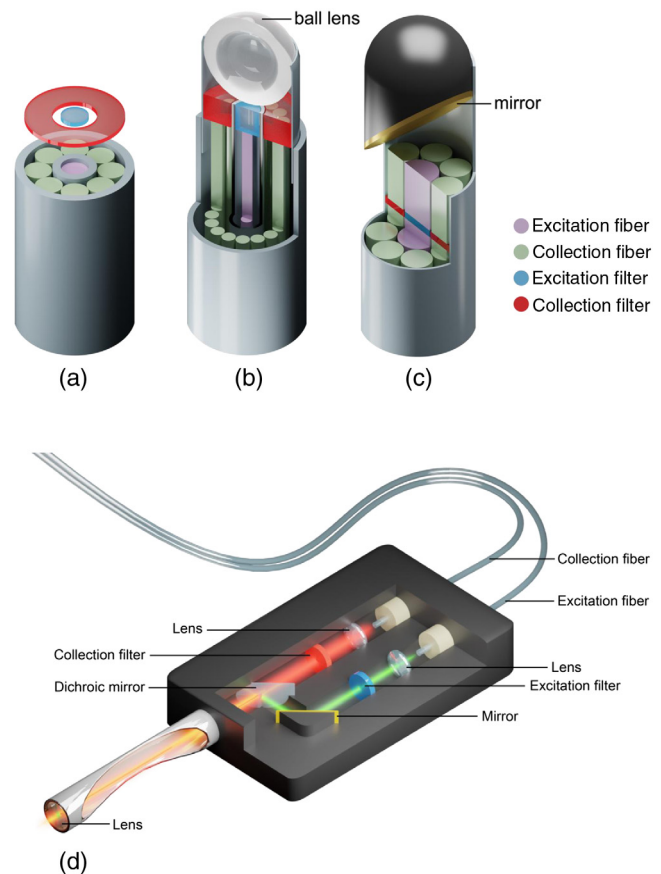

Fig. 2 Different fiber optical Raman probes. (a) Basic endoscopic probe, (b) with ball lens for focusing, (c) with side-view option, and (d) handheld Raman probe.

the tissue by an NIR-coated sapphire ball lens to a focal spot diameter of ∼0.2 mm. The lens is mounted on the tip of the Raman probe and has a diameter of 5 mm. This probe and the more compact version,[38] with a total outer diameter of 8 mm were used for *in-vivo* cervical tissue measurements,[37,39] as well as measurement of the oral cavity.[40] Using Monte Carlo simulations, the depth selectivity of ball lens-coupled probes and its dependence on refractive index and diameter of the ball lens have also been demonstrated.[41]

To reduce interference from deeper tissue layers during endoscopy, a beveled confocal fiber optic Raman probe coupled with a ball lens was introduced in Ref. [42]. It was shown that the ratios of the Raman photons collected from epithelium versus stromal depend on the bevel-angle of the fibers.[42] *In-vivo* measurements during endoscopy also revealed that the Raman spectra acquired using the confocal Raman probe are not easily comparable with a volume-type Raman probe[43] because of the different probed tissue volumes. It was found that about 85% of the collected signal arouse from the top 200-μm epithelium layer of the gastric tissue, whereas 15% arouse from a range between 200 and 800 μm. In addition, the beveled Raman probe provides approximately twofold improvements in tissue Raman-to-autofluorescence intensity ratios as compared with the use of a volume Raman probe.[44] Beveled probes were used in a large trial to acquire spectra from 373 patients with different histological subtypes in the upper gastrointestinal (GI) tract and to construct a comprehensive Raman library with >12.000 Raman spectra.[45] For the online analysis of the *in-vivo* spectra, dedicated MATLAB-based software was used with automated data acquisition and spectra preprocessing, allowing also discarding of noncontact spectra.[46] In further trials,[40,47,48] the advantage of using both the high and the low-wavenumber range was shown. A comparative study demonstrates that the Raman spectroscopic technique coupled with beveled fiber optic Raman probe has great potential to enhance *in-vivo* diagnostics of gastric precancer and early cancer at endoscopy,[44] as compared with a volume probe.

Another clinical setup was introduced by Motz et al.,[49] which uses a sapphire ball lens with a 2-mm diameter and a coupled fiber probe with 15 collection fibers.[50] Here, filters deposited on a special glass substrate were used, instead of directly coating the fiber ends.[43] The probe was applied for margin assessment during breast surgery[51] and in combination with a fluorescence/diffuse reflectance probe for skin cancer diagnostics.[52] A commercial handheld fiber probe (InPhotonics, Norwood, Massachusetts) consisting of a 105-μm excitation fiber and a 200-μm collection fiber was used to study cervical[53] as well as oral cancers.[54]

Short et al.[55] introduced a probe intended for lung cancer diagnostics. The probe comprises two filter stages: one set coated at the distal end of the probe, and the other is placed in the parallel light path; see Fig. [3]. In contrast to contact probes of other groups, this noncontact probe had a probe tip to tissue distance of between 5 and 10 mm and was used to generate an excitation illumination spot diameter on the tissue surface between 2 and 4 mm. An *in-vivo* application with the aforementioned probe showed that high-grade dysplasia and malignant lung lesions can be detected with a high sensitivity of 90% and a specificity of 65%,[56] using only the high wavenumber range, i.e., above 2800 cm^{-1}. To accurately indicate the area being measured, a 532-nm guide laser was added and connected to three of the 31 collection fibers.[57]
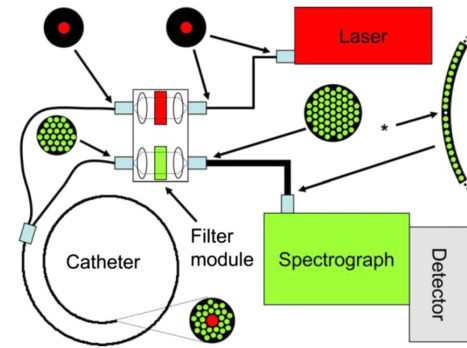

Fig. 3 Schematic diagram of the endoscopic laser Raman spectroscopy system. The inserts show the arrangement of the excitation (red) and collection fibers (green). The collection fibers were connected to the spectrograph through a special round-to-parabolic fiber bundle to correct the spectral imaging distortion. With permission from Ref. [56].

Custom-made commercial probes are also in widespread use. Agenant et al.[58] compared a nonsuperficial (or volume probe)[59] with a superficial Raman probe, both from EMVision LLC[60] (Loxahatchee, Florida) with respect to their sampling range. Both use seven collection fibers surrounding a single excitation fiber. The superficial probe had additionally a two-component converging lens, which is a 1-mm-thick flat window of fused silica, and a proximal element of a plano-convex sapphire lens; see Fig. [4]. This configuration allows overlapping the excitation and collection light at the sample without interference from the sapphire Raman signal and an ∼0.5-mm surface diameter of the sampled region. Using a layered phantom model, they found that the optimal sampling range of the superficial probe is between 0 and 200 μm and for the nonsuperficial probe between 0 and 300 μm.[58] With this range, the superficial probe measures close to the origin of urothelial carcinomas 100 to 200 μm below the surface. It is designed to comply with the regulations of the Medical Device Directive, made of biocompatible materials, and can withstand repeated plasma (STERRAD®) sterilization. With its outer diameter of 2.1 mm, it fits through the endoscopic channel of a cystoscope[58] or a colonoscope.[61] The same type of superficial probe has been used for intraoperative brain cancer detection.[62–64] Using the fiber probe on 17 patients with WHO grade 2 to 4 gliomas, it was possible to accurately differentiate normal brain from dense cancer and normal brain invaded by cancer cells, with a sensitivity of 93% and
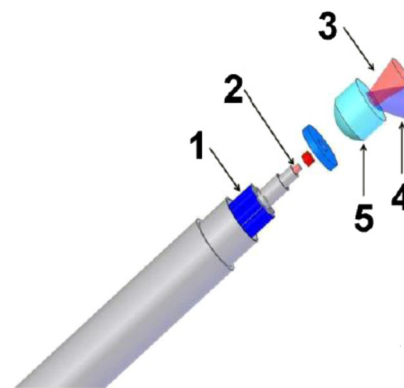

Fig. 4 Superficial probe (1 = 7 times collection fibers, 2 = excitation fiber, 3 = Raman laser cone, 4 = Raman collection cone, and 5 = two-component front lens). With permission from Ref. [58].

a specificity of 91%.[64] The group around Mahadevan–Jansen used this probe to characterize human cervical remodeling throughout pregnancy[65] and inflammatory bowel disease (IBD).[66] For the examination of soft-tissue sarcoma immediately after excision, the slim body of the probe was made pen-like and housed, resulting to an outer diameter of 6 mm.[67] The tissue of 42 patients was measured by bringing the tip of the fiber optic probe in direct contact with the regions of interest, i.e., tumor bed, control of normal muscle tissue, and fat tissue.

Optical filters are usually employed to prevent the reentry of reflected laser light into collection fibers. Another approach is to use a noncollinear arrangement of excitation and collection fibers, which additionally offers advantages concerning the Raman fiber background.[28] The probe was designed as a Raman probe for skin analysis[26,68] and applied with the collection arm perpendicular to the skin surface. To collect the signal 58, optical fibers with a core diameter of 100 μm were used. The fibers are arranged along a curvature and coupled into the spectrometer. As described in Refs. 68 and 69, this probe was used for the detection of benign and malignant skin cancer lesions, respectively. The results published in 2012 showed sensitivities between 95% and 99% and specificities between 15% and 54%.[68] Related patents are licensed to Verisante Technology Inc., Germany, which gained market access in 2011 for the evaluation of suspicious skin lesions in terms of diagnosing melanoma, squamous cell carcinoma, and/or basal cell carcinoma.[70] Another handheld probe for skin measurements[71] was introduced in Ref. 72, additionally containing positioning elements to enable automated positioning of the objective making it somewhat bulky, with an outer dimension of 12.7×20.3 cm. As this handheld system contains no visual imaging capabilities, a targeting system, consisting of a guiding collar with a removable reticle, was developed to allow accurate identification of the measurement location. As for skin applications, a special probe design is not required as the one-around-seven probe from EMVision can also be employed, as was demonstrated in Ref. 73. For skin analysis not related to cancer, but to characterize depth profiles of stratum corneum, e.g., penetration studies of drugs or cosmetic products, in numerous cases a model 3510 Skin Composition Analyzer (River Diagnostics, Rotterdam, The Netherlands) was frequently employed.[74–78]

An alternative miniaturized, confocal fiber optic probe intended to fit within the instrument channel of a standard medical endoscope, with a diameter of 2.8 mm, was developed by Day et al.[36] It was optimized for the study of the carcinogenesis process of esophageal malignancy. The optical layout is related to the probe shown in Fig. 2(d). The group used a monolithic filter/mirror component and developed wet-etched silicon motherboards and the jigs to ensure sufficient positioning accuracy of the optical parts. Although the probe is designed for *in-vivo* application, up to now it has been used to study resected tissues only.[35,79,80] Almond et al.[35] turned it into a contact probe by replacing the aspheric lens with a grin lens.[36]

3.2 Unfiltered Probes

The necessary spectral filtering to suppress the background makes the design and implementation of fiber optic Raman probes for the fingerprint region rather complex. At wavenumbers larger than $\sim$2000 cm^{-1}, the silica core and the cladding of the fiber generate considerably lower Raman background signal. This implies that the costly filters at the distal end of the probes could be omitted if the monitoring would be restricted to the

high-wavenumber range, which was defined in Sec. 2. Hence, the diagnostic properties of the high-wavenumber range in comparison with the full or only the low-wavenumber range have been of significant interest and were widely investigated.[57,81,82] A comparison between the predictive strength of high- and low-wavenumber range was performed using a filtered and an unfiltered probe, respectively.[81] Applying this approach on colon lesions and employing multivariate analyses, the researchers found that detecting the high wavenumber Raman profiles might provide sufficient information for predicting the pathology. This has also been confirmed by others,[83] where a single fiber was used for both excitation as well as collection.

3.3 Spatially Offset Raman Spectroscopy

SORS is a method for the effective retrieval of Raman spectra of subsurface layers in diffusely scattering media and was introduced by Matousek et al.[84] The concept behind SORS is that there is a spatial separation between the point of laser illumination and the point of Raman signal collection on the sample surface.[84,85] There are two main categories: SORS with a central illumination point and a collection ring and inverse-SORS with an illumination ring and a central collection area; see Fig. 5. A method to quantitatively determine the optimal offset for a given chemical sample is introduced in Ref. 86. Commercial devices are available and routinely used for airport security or in pharmaceutics,[87] i.e., for measurements through packages. Starting in 2006,[88] it has been used for *in-vivo* transcutaneous measurement of bone tissue,[89–92] mainly by inverse-SORS. Using a custom-built instrument (Cobalt Light Systems Ltd., Oxfordshire, UK) with offsets of up to 9.5-mm, photon migration properties and Raman signal recovery from the depth within three selected bone types have been assessed.[89] SORS can also be employed for soft-tissue characterization, e.g., for breast tumors beneath a layer of normal tissue.[93–95] An SORS probe for the diagnostics of breast tumors was developed, arranging the collection fibers in four circle segments[94] and not in full circles as shown in Fig. 5. Raman signal collection from three coaxial annuli of optical fibers was demonstrated.[96] In very recent publications,
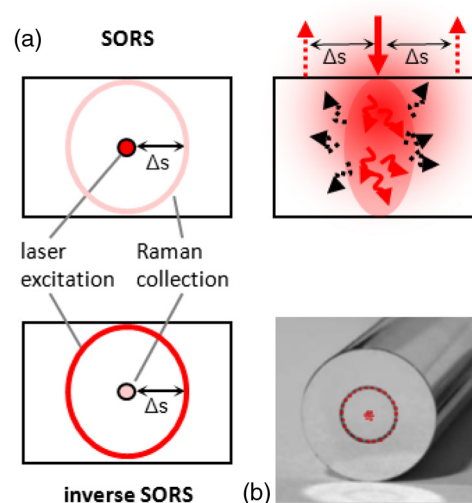

Fig. 5 Spatially offset Raman spectroscopy (a) sketch of SORS and inverse SORS principle and (b) SORS annular fiber probe with an inner and outer ring of collecting fibers. With permission from Ref. 33.

alternative approaches for depth-resolved Raman measurements, namely frequency offset Raman spectroscopy (FORS)[97] and time-domain Raman diffuse spectroscopy,[98] were introduced. With FORS, depth probing can be achieved by exploiting the different values of the optical properties of the medium at different frequencies, whereas time-domain approach exploits differing arrival times of photons.

3.4 Multimodal Probes

Already in 2008, Patil et al.[99] introduced a dual-modal device capable of performing sequential acquisition of Raman spectra and OCT images along a common optical axis. An integrated system with a common sample arm as well as common detection path was also demonstrated.[100] Here, both coregistered datasets are recorded sequentially with the same spectrometer. As a continuation of Ref. 99, the clinical OCT/Raman setup of Patil et al.[101] allowed screening areas of up to 15-mm transverse and 2.4 mm in depth with OCT to identify measurement locations of interest for Raman measurements. However, the overall probe size of $10.2 \times 12.7 \times 20.3$ cm makes it mainly suitable for skin applications. A side-view hybrid probe for *in-vivo* real-time measurements was developed,[102,103] making use of the complementary information provided by OCT and Raman spectroscopy. The handheld OCT/RS probe has a length of ~120 mm with a probe head size of ~13 mm × 8 mm, making it suitable for *in-vivo* tissue measurements on human organs, such as the oral cavity, cervix, and skin, or for intraoperative monitoring, e.g., brain surgeries. With this, both the tissue morphology and biochemical information can be acquired simultaneously *in vivo*. However, making full use of the potential of combined Raman-OCT will require the development of analytical techniques that appropriately correlate the information from both types of data, i.e., imaging and spectroscopy.[101] In Ref. 103, it was demonstrated that the diagnostic strength of the combination is improved in comparison with Raman spectroscopy or OCT alone. To address the issue of obtaining both morphological and molecular information at depth, a hybrid approach integrating OCT with wavelength modulated spatially offset Raman spectroscopy (WM-SORS) was introduced.[104] Using polystyrene in lard phantom, coregistered Raman spectroscopy and OCT measurements at depths of up to 1.2 mm were demonstrated. The wavelength modulation additionally suppresses fluorescence background.[16,105] A Raman-OCT probe for the prospective *in-vivo* clinical melanoma skin cancer screening was integrated into a commercial spectral domain OCT-setup (Telesto II, Thorlabs).[106] To allow a future upgrade with an optoacoustic detector, a pulsed excitation source for Raman spectroscopy was used. For first *in-vivo* measurements, an elliptically illuminated skin area with axes of 9 and 7 mm and integration times of 100 s were used.

Scepanovic et al.[107] developed a multimodal system that combined Raman spectroscopy, autofluorescence, and diffuse reflectance and comprising three light sources that are sequentially coupled to the probe by an optical fiber switch. It was employed for *in-vivo* detection of vulnerable or thrombotic plaques during femoral bypass and carotid endarterectomy surgeries.[108] The ball lens-coupled probe contained a single excitation fiber and a concentric ring of 15 collection fibers, 10 of which were used to collect Raman spectra, and the remaining five to collect reflectance and fluorescence data.

A multispectroscopy surgical probe from EMVision, similar to the probes described in US patents 8,175,423 and 8,702,321,
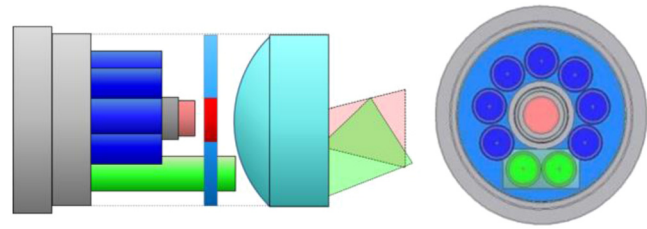

Fig. 6 Schematic view of the probe with filters, lenses, and beam propagation cones. Front view of the probe distal end. The fibers shown in blue are used for collecting the Raman scattering. The fiber shown in red transmits the light for the Raman excitation. The fibers shown in green are for generating the fluorescence/white-light signal. With permission from Ref. 110.

allows sequential acquisition of Raman spectra and fluorescence signals for two excitation wavelengths and the reflection of a white-light source, controlled by an optical switch.[109] Depending on the read-out technique, fluorescence intensity or fluorescence lifetime[110] can be recorded. Figure 6 shows the principal setup, consisting of seven collection fibers around an excitation fiber for Raman spectra and, in green, two fibers for the collection of the other modalities. A multimodal setup, designed for skin cancer diagnostics, was introduced in Ref. 111. It is nearly identical to the probe shown in Fig. 7, except that three fibers with a 200-μm-core diameter are arranged in a triangle and used for fluorescence and diffuse reflectance spectroscopy (DFS). In addition, eight fibers, i.e., seven 300-μm-core collection fibers and one 200-μm-core excitation fiber, are used for Raman spectroscopy. Another difference is that three "non-Raman" fibers bypass not only the donut-shaped longpass filter but also the front lens to correct for spectral aberrations.

3.5 Image Guidance

Recent developments in biomedical Raman spectroscopy indicate that image guidance for Raman measurements is highly advantageous, especially with regard to future computer-assisted and robotic surgery. In Ref. 113, integration and visualization of an image-registered Raman probe were demonstrated. It was shown that the position of the probe can be tracked and registered to any imaging modality, e.g., computed tomography (CT) scans. During brain surgery, a navigation attachment (Medtronic SureTrak) was used for spatial registration with the Medtronic StealthStation system, enabling MR guidance of measurement and tissue sample collection locations.[62,64] A commercial Raman probe from EMVision LLC was adapted to the ARAKNES[114] robotic platform and tested using tissue samples. The final intent is to identify ambiguous tissue margins during robot-assisted endoluminal surgeries.[115] As Raman probes can only perform single-point measurements, the knowledge of the exact measurement point is of great importance[116] because the samples are often very heterogeneous. Schleusener et al.[117] have, therefore, designed a macroscopic Raman probe with a video-recorded measurement spot. Image guidance is also very advantageous for endoscopy as it helps to correlate the Raman measurements with histopathological findings. In 2009, Huang et al.[43] introduced image-guided endoscopy in combination with Raman spectroscopy (Fig. 8). The group used a trimodal widefield setup, i.e., white-light reflectance (WLR), autofluorescence, and narrow-band imaging in combination with point-wise
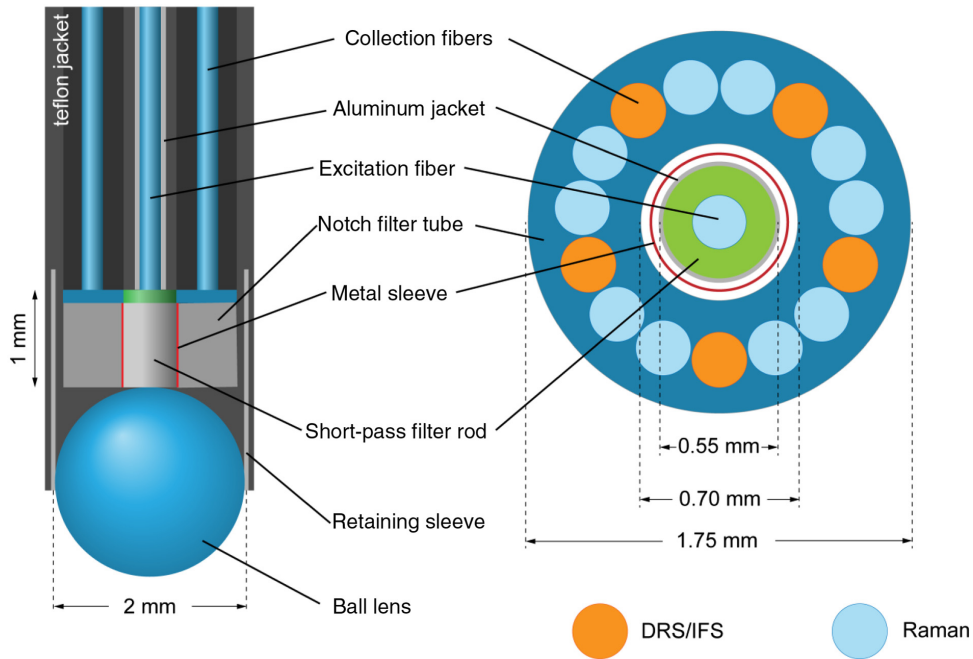
Fig. 7 Schematic of the multimodal spectroscopy probe with a side view on the left and a cross sectional view on the right. A central excitation fiber 200-μm core diameter, 0.22 NA is the surrounded by 15 collection fibers, 10 of which collect Raman spectra and five of which collect DRS/IFS return light. The probe tip contains a module to filter the excitation and collection light and a sapphire ball lens to optimize collection. Adapted from Ref. 107.

Raman measurements. A Raman endoscopic probe with an outer diameter of 1.8 mm was constructed to fit through the instrument channel of a medical endoscope. This is a more direct approach as compared with MR or CT guidance. Confocal, as well as volume probes, can be employed, as long as the size restrictions given by the instrument channel are observed. The Raman probe developed by Huang et al.[43] consisted of 33 optical fibers: one for excitation and 32 for Raman signal collection. The distal end of the fiber probe was coated with two different types of filters; the central excitation fiber is coated with a narrow bandpass filter, centered at 785 nm, with an FWHM of ±2.5 nm. The surrounding collection fibers were coated with edge longpass filters and a cutoff at 800 nm. The Huang-group has published several papers, using the described Raman probe for a variety of *in-vivo* applications.[46,82,118–121] For example, to construct a spectral database to build a model for gastric cancer diagnostics, they acquired 2748 spectra of gastric tissue from 305 patients *in vivo* using the described real-time system.[46] To get a universal tool, organ-specific diagnostic models were implemented,
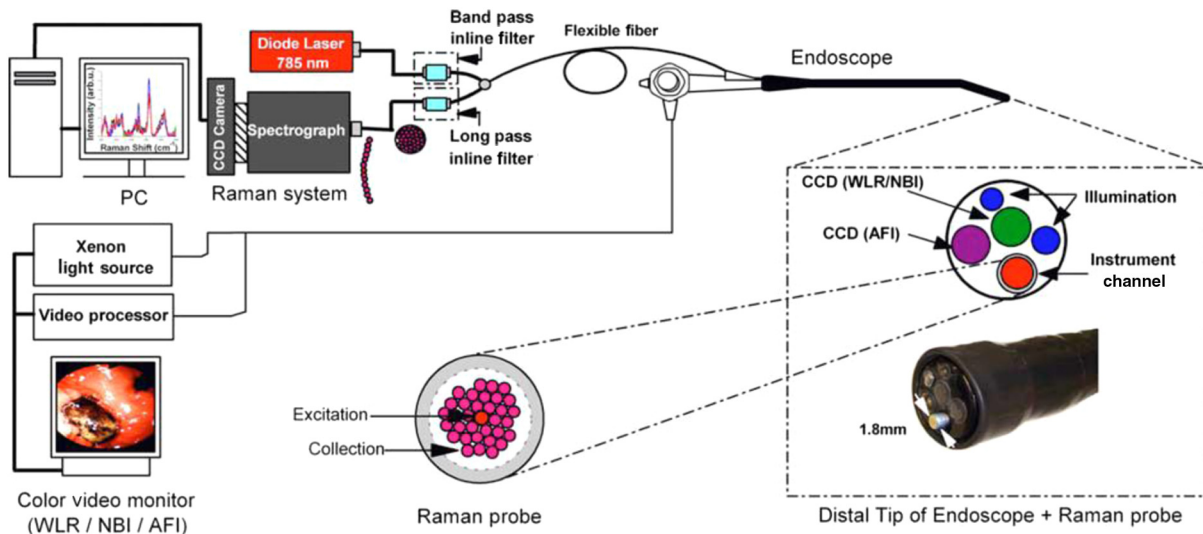

Fig. 8 Schematic of the integrated Raman spectroscopy and trimodal endoscopic imaging system developed for *in-vivo* tissue Raman measurements at endoscopy. With permission from Ref. 43.

enabling instant switching among the spectral databases of different organs, e.g., esophagus, gastric, colon, cervix, bladder, lung, nasopharynx, larynx, and the oral cavity, including the hard palate, soft palate, buccal, inner lip, ventral, and the tongue.[46] This instrumental setup was also used with a confocal probe and improved depth resolution for the characterization of nasopharyngeal cancer.[48] In this study, spectra from 95 patients were recorded. As biopsies were taken only from suspicious sites, relying on otolaryngologists' observations, the researchers state that the "healthy baseline" may not be fully corrected, which could result in errors in tissue Raman classification.[48] More clinical information regarding the mentioned publications can be found in Sec. 4.

3.6 Clinical Use

Several technical challenges remain for clinical use, such as a robust control over the laser radiation dose and measurement repeatability during endoscopy. A decrease in the SNR, due to the aging of the Raman probe after repeated cycles of harsh reprocessing procedures, is also of concern. To address such issues, disposable, biocompatible, and sterile sheaths for manufacturing endoscopic fiber optic Raman probes is being designed and tested.[115,122] Sterilization is realized mostly by either cold gas ethylene oxide or Sterrad R (Advanced Sterilization Products, Irvine, California).[58,108]

To save costs, unfiltered probes have also been investigated and would make single-use probes more feasible as reprocessing can damage the probe or alter its spectral behavior.[81] For some applications, a large excitation spot is preferred as a larger laser intensity can be used while still complying with the maximum permissible exposure (MPE) guidelines.[122] However, a lack of precision in controlling the sampling distance was anticipated under most operating circumstances. Using an EMVision Raman probe[117] with an added light suppression shield, Schleusener et al.[12] investigated the perturbation factors in the clinical surrounding, such as ambient light, contact force, and immersion fluids. Also, user induced, e.g., caused by varying contact force and angle, and system-induced variabilities were investigated.[123] Using an unfocused seven-plus-one probe (EMVision), only small user influence was observed.

During surgery, there can be interference from light sources, as for example, surgical spotlights, white-light sources, and LCD-monitor light. The same holds true when combining Raman systems with image guidance. Spectral interference from the imaging light, which gives rise to spectral artifacts, can easily obscure the weak Raman signal and reduce the predictive accuracy of the analysis. Switching the imaging light off during a Raman measurement increases the risk of puncturing the tissue, and the point of spectral acquisition cannot be visually confirmed.[57] Desroches et al.[63] more thoroughly researched the impact of surrounding light and found arrangements, which avoid measurements in complete darkness, i.e., standard operating room lights can be left turned on as long as they are pointed away from the sample. In a follow-up publication,[124] a filter adapter for the surgical microscope composed of two shortpass filters was designed. This adapter in combination with background removal efficiently suppressed the interference of the operating microscope light source.

Depending on the clinical surrounding, special approaches are necessary. For Raman measurements during interventional MRI, a special fiber probe is needed, with no metal parts in the probe head. Ashok et al. developed an MRI compatible fiber optical Raman probe with a disposable probe head, which also maintains sterility. To make the probe head a single-use component, the filtering was decoupled from the head and the commonly used steel capillaries were replaced by a heat-shrinkable sleeve.

Furthermore, efficient calibration procedures have to be applied to ensure reproducible system performance. Wavenumber calibration is typically accomplished using calibration standards,[109] such as acetaminophen, naphthalene, and a calibration light source. The spectral system response can be calibrated using a tungsten-halogen lamp.[67,111] For quantitative analysis of *in-vivo* tissue, Raman measurements in real-time univariate[125] or multivariate[126] reference signals can be used.

4 Medical In-Vivo Applications

Raman spectroscopy has been used extensively for the characterization of *ex-vivo* biopsy samples; however, the real benefit of the method can only be explored through *in-vivo* applications. As such, there has been a significant movement from *ex-vivo* to *in-vivo* studies in recent years. This section presents the latest *in-vivo* studies and applications of Raman spectroscopy as a potential tool for intraoperative assistance and for the medical diagnostics on a variety of diseases and tissue types, such as cardiovascular and inflammatory disease and lung, breast, digestive and urinary tract, brain, and skin cancer.

4.1 Cardiovascular Diseases

Cardiovascular diseases are the leading causes of death worldwide.[127] Due to the aging of blood vessels lining, the inner walls of arteries become susceptible to deposition and permeation of various lipids circulating through the bloodstream, resulting in a clogging of the vessel walls, a disease which is called atherosclerosis (AT). The associated swelling can severely reduce the blood flow and thus the nutritional supply of the affected organs, which is one of the leading causes of cardiovascular events.

Apart from diagnosing the presence of atherosclerotic plaques, it is well-known that the severity of a plaque and its stability are strongly correlated with its biochemical composition.[128] For instance, the identification of vulnerable plaques remains one of the most important and challenging aspects of cardiology. There are several types of vulnerable plaques, which have distinct biochemical compositions that are characterized by lipid cores, thin fibrous caps infiltrated by macrophages, proteoglycan matrices in a smooth muscle cell-rich environment, intraplaque hemorrhage, or calcified nodules protruding into the vessel lumen.[129] Thus, specific information about the composition of a plaque would greatly improve the risk assessment and management.

Several spectroscopic techniques based on near-infrared absorption, Raman spectroscopy, or fluorescence are currently under investigation or being developed.[130] Due to a high-molecular specificity and sensitivity for lipids and crystalline calcium, which are the main constituting biochemical components of atherosclerotic plaque, Raman spectroscopy is a predestined tool to perform this characterization. Furthermore, it is readily possible to distinguish between subclasses of lipids, such as triglycerides, cholesterol, and different cholesterol esters. The coupling of Raman spectroscopy to miniaturized probes allows a catheter-based implementation that can be

performed during a routine catheter administered cardiovascular intervention, such as stenting or balloon-induced angioplasty. The development of miniaturized Raman probes would allow a combination with cardiac catheterization and could potentially facilitate the diagnosis. It can also be combined with other intravascular imaging techniques.

First, *in-vivo* experiments were reported as early as 2000 on lipid plaque observed in sheep.[131] In 2006, Raman spectroscopy was tested during carotid endarterectomy and femoral artery bypass surgeries.[132] Experiments in combination with other spectroscopic techniques, in particular with DRS and autofluorescence, often referred to as intrinsic fluorescence spectroscopy (IFS),[108,133] demonstrated that Raman spectroscopy is very sensitive to lipid pools. Concurrently, obtained DRS data have been related to the presence of β-carotenoids and superficial foam cells. Autofluorescence, on the other hand, has been used to detect the thickness of fibrous caps. Depending on the Raman probe design, the currently available Raman probes for cardiovascular applications are about 1 mm in diameter, which is generally subject to improvement. At this point, it is noteworthy to mention that Raman excitation within the NIR is not hindered by the presence of blood, and the intensity of the occurring autofluorescence is not too high and does not obscure relevant Raman signals.[134]

In contrast to other modalities, Raman spectroscopy offers enormous benefits because of its potential to provide quantitative data. Early on in cardiovascular applications with Raman spectroscopy, it has been demonstrated that individual plaque components can be quantified. Because of unique compositional parameters, different plaque types can be analyzed in a nonsubjective manner that can assist in the recognition of vulnerable plaques and improve the aforementioned risk management. It is also possible to combine Raman spectroscopy with OCT for fast image contrast on the plaque morphology. *In-vivo* Raman spectroscopy in combination with OCT has been applied consecutively on rabbits (Fig. 9).[112] The allocation of the collected OCT and Raman data can be assured by X-ray angiography during the operation; however, a probe that allows both modalities would be of significant impact. The OCT images and the Raman spectral information of distinct abnormal positions of early plaque formations were recorded. The morphology of early plaque formations was characterized by the OCT images and the Raman data obtained clearly showed the lipid nature of the depositions. All reported studies, mostly *ex vivo*, focused on proof of principle experiments. In particular, the application of Raman probes within arteries under *in-vivo* conditions is still very basic. The current challenges are predominantly of a technical nature, i.e., to design Raman probes that fulfill the technical requirements for applications in human.

Intravascular FLIM has also been compared with Raman spectroscopy. Both modalities were simultaneously acquired from two human coronary specimens using a bimodal probe.[135] Raman spectroscopy could distinguish lipid from necrotic cores, whereas FLIM extracted information could identify fibrous caps.

4.2 Inflammatory Diseases

Inflammatory diseases are linked to a vast array of disorders characterized by inflammation and include allergic asthma, autoimmune disease, hepatitis, and IBD, among others. The diagnosis of inflammatory changes is crucial for the early diagnosis and treatment of autoimmune infections and metastatic
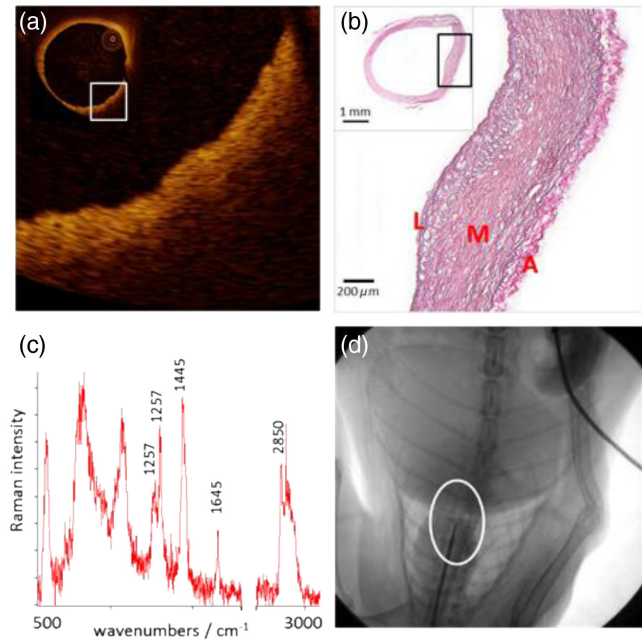

Fig. 9 Enlarged OCT image (a) from the section shown in comparison with an EvG stain (b) of a section from the same region; L, lumen or artery; M, muscularis media; A, adventitia. Graph (c) shows a Raman spectrum with characteristic lipid bands collected within the region, where the OCT image was obtained. The position of the Raman probe is shown in (d). Reprinted with permission Matthäus et al., "Detection and characterization of early plaque formations by Raman probe spectroscopy and OCT: an *in-vivo* study on a rabbit model" with permission of the *Journal of Biomedical Optics*.[112]

diseases.[136] *Ex-vivo* Raman-based diagnostics of asthma and hepatitis was investigated by analyzing serum and blood plasma samples.[137,138]

Ulcerative colitis (UC) and Crohn's disease are two distinct types of IBD. The ability to endoscopically, pathologically, and radiologically diagnose and analyze the disease severity still needs improvement.[139] The potential of Raman spectroscopy to detect molecular alterations in UC and Crohn's (CC) has already been demonstrated.[140] Pence et al.[141] tested a colonoscopy-coupled Raman fiber probe on 53 patients. Raman spectra were collected from the cecum, transverse, and sigmoid sites of the colon with integration times of 0.5 s and an excitation power of 80 mW. To improve the signal collection, a shallow focus design through a focusing microlens at the probe tip was implemented.[142] The authors employed a sparse multinomial logistic regression algorithm to discriminate between UC and CC. The model was based on a Bayesian machine learning framework of statistical pattern recognition and allowed an overall classification accuracy of 95%. Recently, Pence et al.[66] reported a pilot *in-vivo* Raman study to characterize IBD in 23 patients including healthy subjects that underwent a routine surveillance and evaluation colonoscopy, with biopsies collected. The classifiers did not achieve optimal sensitivity and specificity, with 62% and 22%, respectively, when discriminating colitis from the quiescent disease. Nevertheless, the analyzed Raman spectra provided enough information to discriminate between IBD and normal colon, demonstrating the potential of Raman spectroscopy for providing unknown biochemical information that can be used as a diagnostic tool for IBD.

4.3 Cancer

4.3.1 Lung

Lung and bronchus cancers are the most common causes of cancer deaths worldwide,[143] and smoking is the leading cause for this kind of cancer.[144] Techniques, such as CT, chest X-ray, and sputum cytology, are commonly employed for lung cancer screening, but by the time of diagnosis in more than half of the patients the cancer has already metastasized. Early detection is urgently required to allow appropriate treatment and a reduction of mortality rates.[145] For example, using low-dose CT scanning, it was demonstrated that screening a high-risk population for lung cancer has led to a mortality reduction.[146,147] White-light bronchoscopy has also been tested for early detection of cancer. However, it was reported that this technique cannot diagnose early cancers and precancerous lesions, such as angiogenic squamous dysplasia and squamous cell carcinoma *in situ*, and only 29% carcinoma *in situ* (CIS) and 69% of microinvasive tumors were detectable.[148] Fluorescence bronchoscopy has been tested and remains a promising tool for early detection of lung cancer.[149] Nevertheless, a main limitation is the specificity and the ability to only detect the proximal bronchial tree.[150] Early *ex-vivo* and *in-vivo* Raman studies demonstrated the potential of Raman spectroscopy to differentiate accurately tumor from healthy tissue.[151,152] Recently, McGregor demonstrated that Raman spectroscopy together with multivariable analysis allowed differentiation of high-grade dysplasia and malignant lung lesions from tumor tissue and benign lung lesions with a high sensitivity and good specificity for 280 tissue sites of 80 patients.[56] The authors acquired Raman spectra mainly from the high wavenumber region (2775 to 3040 cm^{-1}), with an acquisition time of 1 s. It was observed that spectra with malignant lesions presented a distinctive loss in lipid at 2850 cm^{-1}. The analysis of this vibrational band allowed the discrimination of tumor from normal tissue with a sensitivity of 90% and specificity of 65%, respectively. It was further shown that the low specificity could be improved when Raman spectroscopy was combined with autofluorescence and white-light bronchoscopy.[153] Thereby, the efficiency of Raman spectroscopy has been demonstrated for lung and bronchus cancers detection. Nevertheless, so far it remains investigational and larger clinical trials are required to validate its effectiveness in the early cancer diagnostics.

4.3.2 Breast

The second most common cancer and one of the most frequent malignancies in women worldwide is breast cancer, with 1.7 million new cases per year.[154] Many diagnostic methods have been investigated to diagnose early-stage breast cancer, including MRI, ultrasonography (US), positron emission tomography (PET), and CT, and are routinely used in the clinics.[155] Nevertheless, the sensitivity for the detection of early-stage breast cancer is rather low, and a intrasurgical assessment of the tumor margins is often quite challenging. In addition, there are cost and time constraints that still need to be addressed, and these create a demand for highly-sensitive and rapid methods to assess tumor margins during the surgery of early-stage breast cancer.[155,156] An early study employing 321 Raman spectra from 44 patients demonstrated the potential of Raman spectroscopy to effectively diagnose early-stage breast cancer with a sensitivity of 72% for malignant tissue and 62% for benign

tissue and a specificity for normal tissue of 83%.[157] The authors found that the normal tissue exhibits characteristic bands of carotenoids at 1150 and 1520 cm^{-1}, which can be assigned to C─C and C═C stretching vibrations, respectively. Other characteristic changes were observed in the symmetric and asymmetric C─H vibrations at 2850 and 2940 cm^{-1}, respectively, which are representative of lipids. These characteristic bands were not observed or did exhibit altered appearance in malignant breast tumor tissue. In addition, the group found that the fatty acid composition in cancerous breast tissue had an increased content of 20-carbon essential fatty acid, which is significantly different from the fatty acid profiles present in normal breast tissue. This was also observed by Abramczyk et al.[158,159] after testing the Raman same system on 150 patients. One possible interpretation is that the noncancerous tissue is dominated by monounsaturated oleic acid.[159] Saha et al.[160] reported on the potential of Raman spectroscopy for the real-time identification of microcalcifications as an early sign of breast cancer during stereotactic breast core needle biopsies. The study included *ex-vivo* Raman measurements from 159 tissue sites of 33 patients to detect microcalcifications in breast tissue biopsies. Using a probe described by Motz et al.,[50] the authors employed ordinary least squares fitting to approximate the acquired spectra with a breast model that was developed in a previous study.[161] The authors showed that it was possible to distinguish the types of microcalcifications based on the presence or absence of vibrational bands characteristic of calcium oxalate at 912 and 1477 cm^{-1}; see Fig. 10(a). The specific location in the biopsy from where the spectrum was acquired is shown in Fig. 10(b). In contrast, Fig. 10(c) highlights the prominent band 960 cm^{-1}, which is characteristic for calcium hydroxyapatite/(microcalcification type II). The specific location in the biopsy is shown in Fig. 10(d).

Additionally, Horsnell[162] and Haka et al.[163] evaluated the potential of Raman spectroscopy for *in-vivo* diagnostics for breast cancer. Both report on the feasibility to use the method in an operational theatre environment during surgery. The study by Haka et al. included nine patients and 31 Raman spectra were acquired. With their classification model, they reached an overall accuracy of 93% (28 of 30).[51] The work by Horsnell et al.[162] included 38 lymph node samples from 17 patients, achieving sensitivities and specificities of 90% in unsupervised test. The classification algorithm, as the one applied here described by Li et al.,[164] was able to classify the normal from tumor biopsies with a sensitivity of 94.9% and a specificity of 93.8%.

During the last 5 years, there have been no further records of *in-vivo* studies using Raman spectroscopy for the detection of early breast cancer.

4.3.3 Digestive and urinary systems

According to the international agency for research on cancer, one of the most commonly diagnosed cancers worldwide is colorectal cancer with 1.4 million cases per year. The third most frequent cause of cancer death is stomach cancer with 0.7 million cases (8.8%),[165] while esophageal cancer is the eighth most frequent cancer (3.2%) and the sixth most common cause of death (4.9%).[166,167] The research group around Huang has widely performed *in-vivo* studies with Raman spectroscopy to differentiate normal and tumor tissue in colon, stomach, and the esophagus.[46,47,119,121,168–172] Early work by this group demonstrated the potential of Raman spectroscopy in the stomach by differentiating dysplasia from normal tissue. The authors use
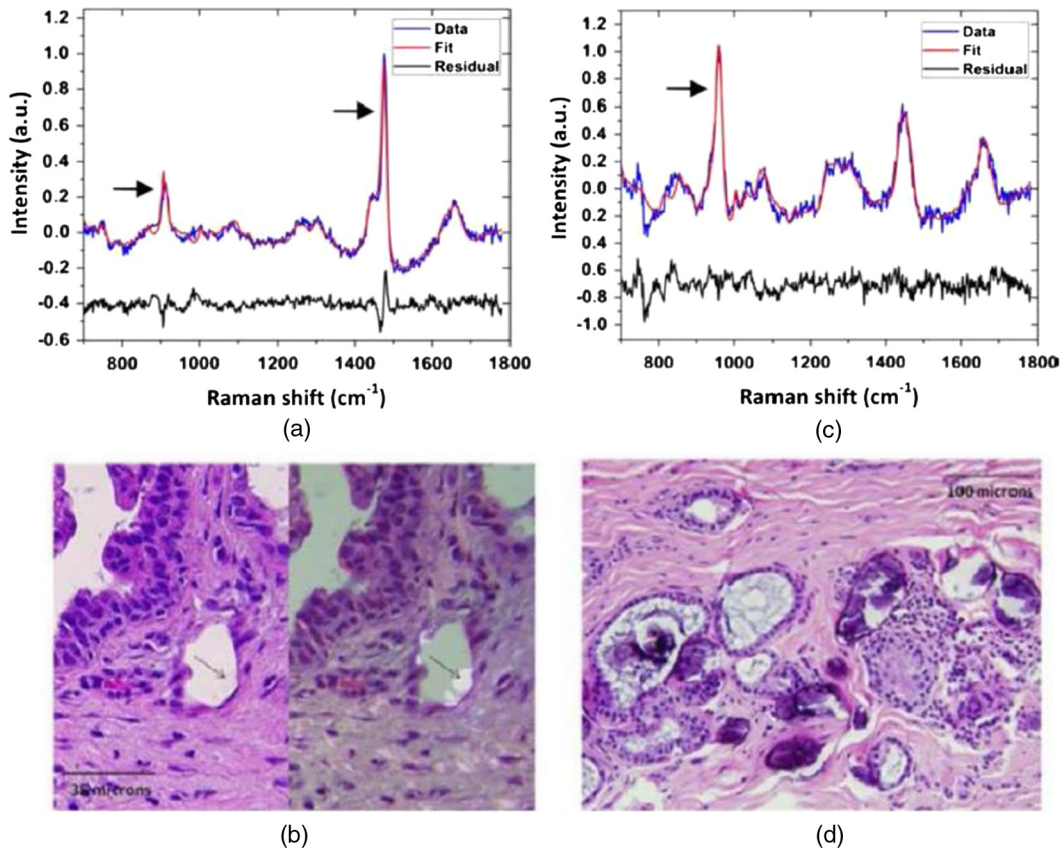
(a)

(c)

(b)

(d)

Fig. 10 Raman spectra and histopathology of breast lesions with types I and II microcalcifications. (a) Microcalcifications type I shows bands at 912 and 1477 cm^{-1}, (b) shows the calcium oxalate crystals (type I), left panel do not bind H&E and right panel viewed under polarized light, (c) Raman spectrum of type II microcalcifications with bands at 960 cm^{-1}, and (d) calcium hydroxyapatite appear as basophilic concretions on the H&E stain. Reprinted from A. Saha et al., "Raman spectroscopy: a real-time tool for identifying microcalcifications during stereotactic breast core needle biopsies" with permission of *Biomedical Optics Express* (OSA).[160]

a 785-nm excitation laser and measured 76 gastric tissue samples from 44 patients, with 55 normal tissue samples and 21 tissue sample exhibiting dysplasia.[173] Data were analyzed by the variation in the band intensity ratio at the band 875 cm^{-1}, i.e., C—C stretching of hydroxyproline, and the band at 1450 cm^{-1}, i.e., CH$_2$ bending of proteins/lipids, resulting in a sensitivity of 85.7% and a specificity of 80%.

Huang and Bergholt[174,175] have also performed *in-vivo* Raman measurements in the stomach for a label-free diagnostics of epithelial neoplasia, benign, and malign stomach ulcers. The results of these studies demonstrated that the diagnostic capability is optimized through the combination of near-infrared autofluorescence with Raman spectroscopy. A total of 1098 normal tissue and 140 cancer gastric tissue samples from 81 patients were measured with a spectral acquisition time of 0.5 s. The differentiation between gastric cancer and normal tissue was achieved with a sensitivity of 97.9% and specificity of 91.5%. The main advantage of combining Raman spectroscopy with autofluorescence is that the latter provides additional information, such as changes in morphological structures, tissue scattering, absorption, and endogenous fluorophore content of sample.[121] Bergholt et al.[119] also performed *in-vivo* diagnostics of esophageal cancer with image-guided Raman endoscopy by combining widefield endoscopic imaging, narrow band imaging, and autofluorescence imaging in 75 esophageal tissue sites from 27 patients, where 42 Raman spectra were acquired from normal tissues. It was found that the esophageal cancer tissue exhibits Raman bands associated with cell proliferation, lipid reduction, and neovasculation. The LDA-based diagnostic model allowed differentiating tumor from normal tissue with a sensitivity of 97% and specificity of 95%. Examples of *in-vivo* Raman spectra and Raman difference spectra of normal and cancerous esophageal tissue from this publication are plotted in Fig. 11. The difference spectra between the distal and proximal esophageal sites of normal tissue show insignificant detectable biomolecular variability; see Fig. 11(b). Figure 11(c) shows the difference spectrum between tumor and normal esophageal tissue, which resolves meaningful biomolecular changes that are related to neoplastic tissue transformation.[176,177] Other relevant studies on the esophagus, although *ex vivo* but worth mentioning, were carried out by the Stone's group.[79,80] Kendall et al. performed the diagnostics of esophageal cancer using a Raman probe on 123 esophageal biopsies collected from 49 patients. The authors demonstrated that high levels of sensitivity (81%) and specificity (98%) can be achieved using the miniature confocal fiber optic Raman probe at 50 mW, laser excitation of 830 nm, and acquisition times between 2 and 10 s from random locations on the surface of each sample.[36,79]

Recently, Wang et al.[171] demonstrated that the acquisition of both the low and the high wavenumber regions of a Raman
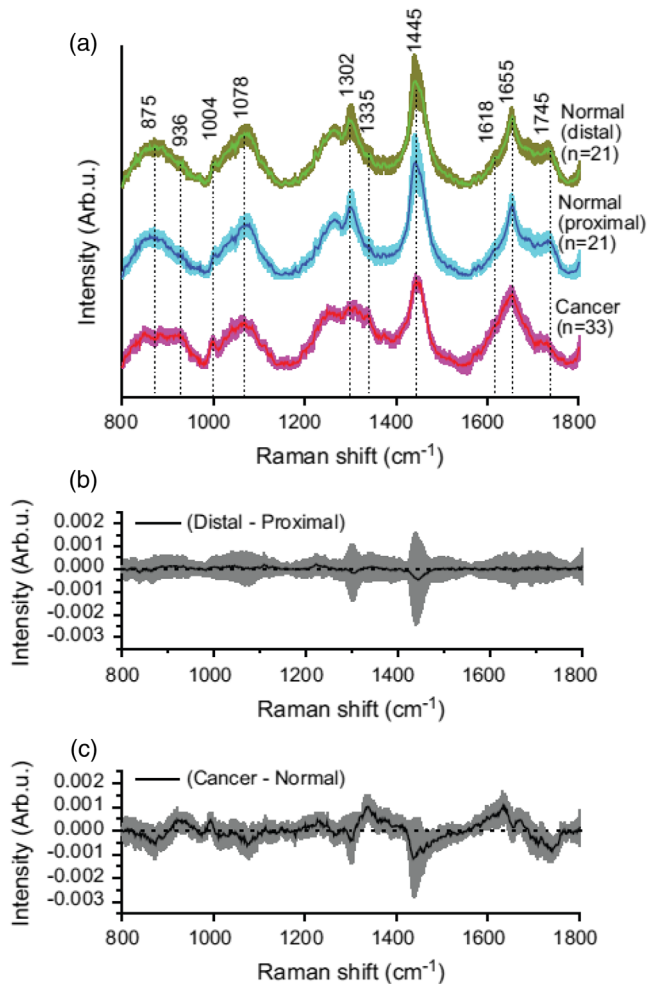
Fig. 11 (a) Mean Raman spectra obtained *in vivo* and standard deviations of normal and cancerous esophageal tissue, the spectra are shifted vertically to observe easily the change, (b) The difference spectrum of the mean normal Raman spectra between the distal and proximal esophageal tissue, and (c) difference spectrum of the mean Raman spectra between cancer and normal esophageal tissue. Adapted with permission from Bergholt et al., "*In-vivo* diagnosis of esophageal cancer using image-guided Raman endoscopy and biomolecular modeling" with permission of the *Journal of Technology in Cancer Research and Treatment*.[119]

spectrum meaningfully enhances the detection of esophageal neoplasia *in vivo* in comparison with each region alone. The authors measured Raman spectra from 48 esophageal patients under endoscopic examination, with 80% of the data used to train a model and the remaining data used for testing the data acquired with a confocal beveled fiber optic Raman probe.[42] The classification was performed using partial least squares discriminant analysis with cross validation, resulting in a diagnostic sensitivity of 97% and specificity of 97.4% of the esophageal squamous cell carcinoma. The changes were attributed to a reduction of the Raman band intensities at 1078 cm^{-1}, which is associated with a reduction in lipid content that occurs mainly due to the thickening of the cancerous esophageal mucosa.[178] In a follow-up study, Wang et al.[47] also reported an *in-vivo* investigation into diagnostics gastric dysplasia, mostly known as a precursor of gastric cancer. The authors tested the fiber Raman probe system employed in the previous study[45,171] to differentiate normal, dysplastic, and

cancerous gastric tissue, achieving much higher specificity in comparison with WLR endoscopy, 95.9% and 51%, respectively. The study obtained a total of 5792 Raman spectra of gastric tissue, i.e., 89% normal, 2% high-grade dysplasia, and 8% adenocarcinoma from 191 gastric patients and 441 tissue sites. Bergholt et al.[179] also reported for the first time depth-resolved Raman endoscopy as a tool for the *in-vivo* detection of dysplasia in Barrett's epithelium, with a total of 43 patients that were tested with Raman endoscopy. The fiber optic Raman probe was used in direct contact with the GI epithelia. The Raman signal was acquired from a layer of a depth of ∼200 μm, with a 785-nm excitation trimodal Raman spectroscopic platform, which allowed the resolution of histopathological features of endogenous biomolecules in the epithelium.

Lin et al.[172] reported diagnosing gastric intestinal metaplasia (IM) *in vivo* using the beveled fiber optic Raman probe previously developed.[42,44] The authors acquired 4520 gastric Raman spectra from 157 gastric patients, i.e., normal 92% and IM 8%. Relevant differences between normal and IM tissue were reductions in the band intensities at 875 and 1078 cm^{-1}, which are associated with collagen and lipid contents, respectively.

Bergholt et al.[180] demonstrated in 2015 in an *in-vivo* study that specific biomolecular variations picked-up by Raman spectroscopy in different anatomical locations within the colorectum of normal colorectal tissue is negligible compared with cancer tissue.

The authors acquired Raman spectra from 1129 sites of five different locations, i.e., ascending colon 16%, transverse colon 22%, descending colon 11%, sigmoid 19%, and rectum 32%, in 50 patients. To complement this work, Ding et al.[181] investigated different physiological factors on biochemical properties of colon tissue. After measuring 455 Raman spectra from 56 subjects, between 28 and 85 years of age, it was found that ethnicity, gender, and age in relation with body mass index (BMI) are key factors of variability in the spectra within the normal tissue, mainly from contrasting abundance between lipids and proteins. The authors report that the intensity of Raman bands at 1303, 1445, and 1656 cm^{-1} increased substantially in obese and overweighed patients compared with the normal subjects. In contrast, protein decreased in both groups. It is, therefore, reasonable to consider the BMI a relevant factor when applying Raman spectroscopy for label-free *in-vivo* diagnostics.

Worldwide bladder cancer has become the ninth most common cancer, with a mortality rate of >60%.[182] Early studies on biopsies demonstrated the potential of Raman spectroscopy to detect different bladder tumors (CIS, G1 to G3) from normal bladder tissue.[183–186] For instance, it was found that the DNA content increases for pathologies within the bladder and the prostate, while in contrast the collagen content decreases. In addition, a higher level of cholesterol with an increased severity of the tumor was observed.[187] These investigations were complemented by another *ex-vivo* study that employed confocal Raman probes acquiring 140 Raman spectra from 28 fresh biopsies of 14 patients optimizing the classification algorithm and achieving a sensitivity of 85.7% and specificity of 100% for the diagnostic performance.[185] Further steps were taken by Stone and coworkers[188] in collaboration with Motz et al.[49] The authors reported on a clinical fiber optic Raman system for the discrimination between benign and malignant snap-frozen bladder samples with an overall accuracy of 84%.[50,188] This initial work allowed the translation of the Raman-based diagnostic approach from *ex vivo* to *in-vivo* bladder cancer

diagnostics. A highly cited study on *in-vivo* bladder cancer diagnostics was reported by Draga and coworkers,[59] who performed measurements on 38 patients, using a Raman spectroscopic probe, reported previously by Magee et al.[151] For each sample, a leave-one-out cross validation was used to distinguish cancer from normal tissue, achieving a sensitivity of 85% and specificity of 79%.

4.3.4 Head and neck

Head and neck squamous cell carcinoma (HNSCC) includes a variety of tumors in the lip, oral cavity, hypopharynx, oropharynx, nasopharynx, and larynx. HNSCC is the sixth most common malignancy worldwide,[189] with about 85,000 incident cases and over 50,000 reported deaths from nasopharyngeal carcinoma (NPC) in 2012.[190] As an alternative to the standard tissue biopsy methods, optical spectroscopy techniques, such as light scattering, Raman and fluorescence spectroscopies have been tested for the detection of early-stage NPC.[191–193]

The application of Raman spectroscopy for cancer diagnostics of head and neck has been reported for several cases.[191,194–196] For example, Lin et al.[82] implemented transnasal image-guided Raman spectroscopy in the higher wavenumber region to detect laryngeal tumor tissue with a miniaturized fiber optical Raman probe in the larynx, acquiring 94 Raman spectra with 23% normal and 77% tumor sites from 39 patients that underwent laryngoscopic screening. The measured spectra presented prominent differences between normal and tumor tissue in the Raman band intensities at 2845, 2880, and 2920 cm^{-1} associated with CH_2 stretching of lipids, and the 2940 cm^{-1} band, which is assigned to the CH_3 stretching vibration of proteins. The authors were able to differentiate laryngeal tumor from normal with a diagnostic sensitivity of 90.3% and specificity of 90.9%.

Further studies in the nasopharynx and larynx allowed the first implementation of *in-vivo* real-time transnasal image-guided Raman endoscopy,[116] where the authors employed an earlier described Raman probe[43] to acquire 874 Raman spectra of 60% posterior nasopharynx, 18% of the fossa of Rosenmüller, and 22% true laryngeal vocal cords (LVCs) from 23 patients without any previous carcinosis. The spectra provided characteristic information about the composition and morphology variations in the normal nasopharynx and larynx tissue. The mean spectra of each intersubject nasal track are shown in Fig. 12, where each spectrum was acquired within 0.1 s. The WLR images of the upper (PN), mid (FOR), and lower (LVCs) nasal track are also shown. In another study, the *in-vivo* anatomical variability of the oral cavity was investigated, and Raman spectra from 26 healthy volunteers and 113 patients registered for medical examination without a history of malignancy or dysplasia were acquired. The authors performed unsupervised classification to identify anatomical differences of the measured sites, whereby the anatomical clustering yielded an overall accuracy of 95%.[197] Wang et al.[103] characterized biochemical and morphological changes of clinically relevant locations of oral tissue, i.e., alveolar process, the floor of the mouth, and lateral tongue *in vivo* by combining Raman spectroscopy with optical coherence tomography (RS-OCT). The study was carried out on 26 healthy volunteers with 1049 Raman spectra acquired from alveolar process (31%), lateral tongue (33%), and floor of mouth (36%). OCT images were acquired to reveal the inter-anatomical morphological dissimilarities. Partial least squares discriminant analysis was used to train the dataset
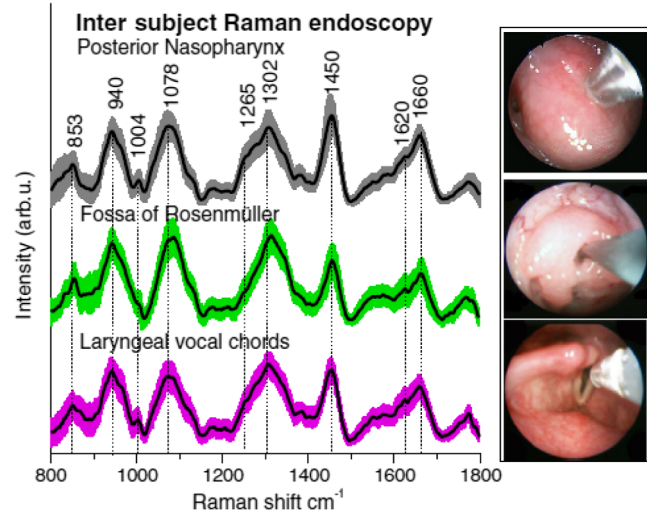

Fig. 12 Mean Raman spectra obtained *in vivo* of posterior nasopharynx (PN), fossa of Rosenmüller (FOR), and LVCs. The mean spectra are oriented vertically. In addition, *in-vivo* fiber optic Raman endoscopic acquisitions from upper-, mid-, and lower-nasal track under WLR and narrow band imaging guidance are presented (Reprinted with permission of JBO).[116]

obtained with the RS-OCT, yielding a higher diagnostic sensitivity of 100%, 76.5%, and 51.3% and specificity of 95.1%, 77.6%, and 89.6%, respectively, than obtained by just using Raman spectroscopy, i.e., sensitivities of 90.2%, 77.5%, and 48.8%, and specificities of 95.8%, 72.1%, and 88.8% for the differentiation of tumor and normal tissue of alveolar process, lateral tongue, and floor mouth, respectively.

Huang and coworkers[42] investigated a micro-optical Raman probe for the *in-vivo* diagnostics of laryngeal cancer, acquiring 2124 Raman spectra, i.e., 62% normal and 38% tumor tissue from 60 patients under routine endoscopic examination. They reported that laryngeal tumor differs from normal tissue and that the changes are associated with the water content in the larynx, as well as the composition of proteins, lipids, and nucleic acids. The measured spectra were analyzed with partial least squares discriminant analysis, achieving a sensitivity of 93.3% and specificity of 90.1% and diagnostic accuracy of 91.1%.[198] In a follow-up publication, the authors also confirmed that observed Raman bands at 940 cm^{-1} for proline and valine and 1078 cm^{-1} for lipids decrease as a consequence of the thickening of the epithelium associated with cancerous progression, which obscures the collagen Raman emission from deeper tissue layers.[199] Furthermore, the group also tested the probe for *in-vivo* diagnostics of nasopharyngeal in 95 patients, acquiring 3731 spectra, 47% of them from normal tissue, and applying PCA-LDA together with leave-one-subject-out cross-validation (LOO-CV), obtaining a diagnostic accuracy of 93.1%.[48]

4.3.5 Brain

Surgical removal of the entire tumor tissue in brain, even meningiomas (benign tumor), is crucial for optimal treatment of the affected patient.[200] US, PET, CT, and MRI allow defining the border for tumor excision.[201,202] However, despite the extended use, even intraoperative MRI, US, and PET have several drawbacks, such as the application of radioactive tracers, spatial resolution, scanning, and patient transport time.[203] A further complication occurs in the correlation between any imaging

Fig. 13 Raman handheld probe being used in the operating room at the Montreal neurological Institute and Hospital by neurosurgeon Dr. Kevin Petrecca. The sources of ambient light can be observed including the microscope white-light, operating room overhead lights, and LCD screens (Reprinted with permission of JBO).[230]

modality performed before a craniotomy and the true location of the brain after the craniotomy. A method that can provide biochemical information to differentiate tumor from nontumor tissue can provide supplemental information to current techniques.[204] The potential of Raman spectroscopy for intraoperative differentiation of brain tumor from normal brain tissue has been evaluated.[205–207] One recent study demonstrates the potential of Raman spectroscopy for intraoperative brain cancer detection. The handheld contact Raman probe (EMVision) (see Fig. 13) was tested on 17 patients by collecting 161 measurements per sample with an integration time of 0.2 s with a laser power between 37 and 64 mW. The researchers were able to distinguish normal brain from dense cancer with a sensitivity of 93% and specificity of 91%, enabling also the detection of brain cancer cells in patients with grade 2 to 4 gliomas.[64,208] The work was partially consistent with previously published results. The samples with cancer cells in comparison with normal brain showed differences in the lipid bands at 700 and 1142 cm^{-1}; the additional changes in the 1540 to 1645 cm^{-1} bands indicate the higher content of nucleic acid in cancer cells.[209] It has to be emphasized that it is crucial to properly correct the signal when strong background from autofluorescence or from ambient light is present. In addition to the significant shot noise level, a convolution of the broad polynomial background with the filter function can easily result in additional peaks and can even emulate to some degree Raman spectra, making the analysis very challenging and the results often misleading. Jermyn and coauthors also demonstrated the potential of boosted trees[109] and artificial neuronal networks (ANN)[210] to distinguish tissue with and without the presence of light artifacts, concluding that ANN achieves an accuracy of 90%, sensitivity of 91%, and specificity of 89% when measuring with light artifacts. In contrast, boosted trees have a lower accuracy.[109] A recent study characterized the SNR of a Raman probe system for intraoperative brain tissue on 10 patients. The authors proved that by increasing the integration time from 0.05 to 0.1 s and reducing the CCD camera temperature to −80°C, the SNR increases by 41% and 35%, respectively, in addition they showed that the system response is linear by relating laser power and integration time with relevant bands ratios. This study also demonstrated that necrosis can be distinguish from tumor and healthy brain tissue with an accuracy, sensitivity, and specificity above 84%;[63] the authors performed the test with an excitation laser operated between

40 and 60 mW at 0.05-s integration time. The probe was sterilized with a STERRAD system in a standard low temperature procedure that uses plasma gas.

4.3.6 *Prostate and cervix*

Prostate cancer is one of the leading causes of cancer mortality among men with 1.4 million reported cases and 293,000 deaths worldwide in 2013.[211] There is a comparable number for cervical cancer with an estimated 266,000 deaths worldwide in 2012.[212] Diagnostic techniques for early detection of cervical cancer, such as screening methods, e.g., pap smear, visual inspection with acetic acid (VIA), and excisional biopsy, have been investigated, but poor sensitivity and specificity have been reported.[213,214] The potential of optical spectroscopic techniques has been extensively studied; for instance, *in-vivo* fluorescence and reflectance spectroscopy have demonstrated sufficient sensitivity at low cost.[215,216] Nevertheless, studies using Raman spectroscopy demonstrated that *in-vivo* diagnostics of cervical cancer with higher accuracy is possible.[39,217] An early *in-vivo* high-wavenumber Raman spectroscopy study on 46 women, using a handheld fiber optic Raman probe coupled with a ball lens, demonstrated that dysplasia tissue could be identified with a sensitivity of 93.5% and specificity of 97%.[37] Comparing Raman spectra of normal and dysplasia cervical tissue, distinct intensity differences were observed at CH_2 stretching bands of lipids (2850 and 2885 cm^{-1}) and at CH_3 stretching bands of proteins (2940 cm^{-1}), respectively.[37] The authors evaluated the intensity ratio of protein to lipid bands, resulting in ratios of 5.05 for dysplasia tissue and a lower ratio of 4.16 for normal tissue. The differences were linked to a decrease in content of membrane lipids, combined with an increase in short-chain fatty acids. Changes induced by dysplasia led to an increase in the nucleic hyperchromatism and density.[219] In one of the first studies, Duraipandian et al.[39] reported an *in-vivo* investigation on cervical precancer detection, using Raman spectroscopy, based on the measurement of 105 near-infrared Raman spectra from 57 sites *in vivo* of 29 patients, with 65 spectra from normal and 40 from cervical precancerous sites. The authors employed a genetic algorithm partial least squares discriminant analysis (GA-PLS-DA-dCV) to identify seven significant bands associated to lipids, proteins, and nucleic acids in tissue and were able to differentiate low and high-grade precancerous lesions with a diagnostic accuracy of 82.9%. To further increase the diagnostic accuracy, the authors also incorporated spectral variations linked to confounding factors, such as age, race, smoking habits, and menopausal status in cervical Raman spectra from previous studies to the GA-PLS-DA-dCV model.[220] The authors also investigated variations in the high wavenumber region aimed to improve the classification accuracy of cervical precancer. The acquired Raman spectra were stratified based on the menopausal status of the cervix of 15 patients, increasing the accuracy from 71% to 91%.[221] A follow-up study by Duraipandian et al.[217] explored the advantages of using both the low- and the high-wavenumber regions for *in-vivo* detection of cervical precancer, acquiring 473 Raman spectra (349 normal) from 35 patients. The researchers observed intensity increases in the bands at 1001, 1095, and 1313 cm^{-1} of dysplastic cervical tissue in comparison with normal tissue. In a second follow-up study, the authors investigated composite NIR AF/Raman spectroscopy for cervical precancer diagnostics. Here, 1240 NIR AF/Raman spectra were acquired *in vivo* from 115 normal sites

of 84 nonpregnant female patients, between 18 and 70 years of age, undergoing a colposcopy revision linked to abnormal pap smears. The combination of near-infrared Raman spectroscopy with autofluorescence yielded a diagnostic accuracy of 84.1% for *in-vivo* discrimination of dysplastic cervix. Nevertheless, the autofluorescence intensity change associated with dysplastic progression was not significant, which indicated that confocal-based NIR AF spectroscopy alone is inefficient for precancer identification.[222] In a further investigation using NIR Raman spectroscopy, the author reported that Raman spectral biomarkers can be used for monitoring the multistage cervical precarcinogenesis at the molecular level.[223] A semiquantitative modeling based on the major biochemical macromolecules in cervical tissue, i.e., DNA, histone, collagen, triolein, and glycogen, contains the stepwise accumulation of biomolecular changes associated with progressive cervical precarcinogenesis.

The potential of Raman spectroscopy for prostate cancer was investigated by Crow et al.,[224] who developed a diagnostic algorithm to differentiate between pathological groups, i.e., benign prostatic hyperplasia and adenocarcinoma-Gleason, with an accuracy of 89%. The authors found reduced glycogen content and increased nucleic acid content in malignant samples compared with benign pathologies. In a follow-up study, the authors also tested an NIR fiber optic Raman system to acquire 220 Raman spectra from 29 bladder samples in cystoscopic procedures and 197 Raman spectra from 38 prostate samples.[188] The developed algorithm differentiated benign prostatic hyperplasia and prostatitis from prostate cancer with 86% overall accuracy. Further studies using Raman spectroscopy reported accurate differentiation of benign and malign prostate tissue.[225] For instance, the differences in the band intensities at 782 cm^{-1} in the cancer samples compared with benign samples can be interpreted as an increase in the DNA content in cancer prostate tissue.[225] *In-vivo* investigations in prostate have not been reported, but the potential of Raman for *in-vivo* prostate cancer diagnostics has been demonstrated and should be expanded to the *in-vivo* diagnostics of prostate cancer.

4.3.7 *Skin*

As one of the most exposed organs of the human body, the skin has been studied and is routinely investigated by various optical modalities. Clinical routine investigations range from large screening dermoscopy and whole-body photography to the assessment of a few atypical and preselected regions that are investigated by pathologists.[70] The gold standard for risk evaluation of skin abnormalities and the diagnosis of skin cancer is based on biopsy extraction and subsequent histopathology, which is usually time consuming. The need for real-time and noninvasive examination of skin abnormalities arises from the growing number of skin cancer cases. Apart from supporting on-site evaluation, fast diagnosis can be beneficial as most skin cancers can be cured if recognized early enough.[226] Several spectroscopy methods, such as Raman, reflectance, and fluorescence spectroscopy, have been widely investigated.[227] Lui et al.[68] have demonstrated the feasibility of Raman spectroscopy in combination with multivariate data analysis to distinguish cancerous from benign lesions, showing promising results for skin cancer. The group used a Raman probe that consists of a 200-μm-core diameter single fiber to collect the generated Raman signal and one fiber to illuminate a 3.5-mm diameter skin area. The collected single-point spectra were recorded in 1 s and subjected to principal component with generalized

discriminant analysis (PC-GDA) and PLS for statistical data evaluation. All together 453 patients were examined, with abnormalities including melanomas, basal cell carcinomas, squamous cell carcinomas, actinic keratoses, atypical nevi, melanocytic nevi, blue nevi, and seborrheic keratoses. The sensitivities to differentiate skin cancers and precancers from benign skin lesions, melanomas from nonmelanoma pigmented lesions, and melanomas from seborrheic keratoses ranged between 95% and 99%. The achieved specificities of about 15% were still higher than that of studies based on inspections by clinicians.[228] Another probe-based approach was suggested by the University of Texas (Austin) in collaboration with EmVision.[111] They employed a seven-around-one fiber optic Raman probe in combination with fluorescence and reflectance measurements. In a clinical study, the group investigated 137 lesions from 76 patients with cases of MM, nonmelanoma pigmented lesion (PL), BCC, actinic keratosis (AK), and SCC.[52] The sensitivity was 100% and specificity values ranged between 95% and 71%, depending on the differentiation between individual abnormalities. The best classification performance for nonmelanoma skin cancer was obtained using multiple modalities. The best melanoma classification was evaluated based on the Raman data alone. To support the data analysis, the group also analyzed the spectral contributions of individual skin components such as collagen, elastin, triolein, nuclei, keratin, ceramide, melanin, and water, by fitting spectra obtained *in vitro* using Raman microscopy.[229] A probe design using 785-nm excitation was used in a larger clinical study involving 104 patients being suspected of having MM ($n = 36$), BCC ($n = 39$), and SCC ($n = 29$).[73] The probe design focuses the excitation beam to a spot size of 104 μm and 17 mW on a sapphire finishing lens surface, which results in an asymmetrical detection spot with dimensions in the range of 500 to 600 μm. The probe was designed for contact mode, and the backscattered light is guided by three 100-μm collecting fibers into the spectrometer. The incorporated lens potentially allows penetration depths of 100 μm or more, which can be crucial to reach the epidermal site of the basal membrane as a potential site of early cancer development. NMSC, MM, and pigmented nevi (PN) were discriminated with high accuracies of 73% for BCC, 85% for SCC, and 91% for the pigmented cases. There have also been approaches to combine Raman spectroscopy with OCT as it is probably the imaging modality that has the best potential to be used as a routine clinical screening technique. The first *in-vivo* experiments were reported in 2011 by the group of Mahadevan-Jansen.[101] The described multimodal setup employs focusing optics for the Raman excitation with an estimated spot size of 44 μm at the sample with a depth penetration of ~530 μm at an excitation power of 40 mW. The Raman spectra of normal skin and BCC were compared and showed significant differences mainly around 1090, 1340, and 1440 cm^{-1}.

5 Summary and Outlook

In-vivo Raman spectroscopy has a great potential to enable noninvasive clinical diagnostics for a variety of diseases because it provides label-free information about the biomolecular fingerprint of the sample and can be used to characterize and to differentiate different disease stages. In the recent years, there have been significant technological achievements and a considerable number of clinical applications readily performed. This review provides a comprehensive overview of the different technical aspects and clinical *in-vivo* applications. It describes

instrumentational aspects, starting with the choice of the appropriate components, such as excitation source, detector, and spectrometer, but it also describes in detail the different fiber optical Raman probes, which have been shown in different experimental settings. Any successful *in-vivo* Raman measurement is tightly bound by the instrumentation parameters and has to be carefully assessed by the developer before measurements can be performed. Instrumentation parameters, such as the linewidth of the laser, the read noise level and dark current of the detector, and the spectral resolution of the spectrometer unit, are just a few that have to be carefully evaluated. Although the performance can usually be ensured by high-end scientific devices, it is also important to emphasize that cost can play a significant role in moving Raman spectroscopy to the clinical environment. It is, therefore, highly important to evaluate how parameters, such as spectral resolution, spatial sampling size, and spectral SNR, can be sacrificed while maintaining adequate label-free clinical diagnostics. The simplification of device structure will ultimately lead to reduction in cost and a wider availability of the method. In addition to the instruments, it is highly important to consider the designs, development, and performance of the specific fiber optic Raman probes. Here, new designs based on fiber technologies have to be addressed and tested to reduce the complexity of constructing Raman fiber probes. This will result in low-cost, single-use probes, which can further help to make Raman spectroscopy an invaluable diagnostics tool. The implementation of Raman-probes tailored to the working channels of commercially available endoscopes has already been shown by several groups. The combination with other spectroscopy and imaging modalities will further expand on the applicability of the method, and additional multimodal probe designs will appear in the near future. The clinical applications outlined in this review clearly demonstrate the great potential for *in-vivo* use of biomedical Raman spectroscopy. Ultimately, as efficiently summarized in Ref. 4, the advantage of Raman spectroscopy over existing medical devices has to be demonstrated in large cohort studies based on patient outcomes and compared with accepted gold standard methodologies. Overall, in the last several years, there has been significant progress in moving Raman spectroscopy from a pure scientific research method to a mature tool, which bears significant promise to provide label-free *in-vivo* diagnostics.

Disclosures

The authors have no potential conflicts of interest to disclose.

Acknowledgments

References

1. E. B. Hanlon et al., "Prospects for in vivo Raman spectroscopy," *Phys. Med. Biol.* **45**, R1–59 (2000).
2. I. W. Schie and T. Huser, "Methods and applications of Raman microspectroscopy to single-cell analysis," *Appl. Spectrosc.* **67**(8), 813–828 (2013).
3. O. Stevens et al., "Developing fibre optic Raman probes for applications in clinical spectroscopy," *Chem. Soc. Rev.* **45**, 1919–1934 (2016).
4. I. J. Pence and A. Mahadevan-jansen, "Clinical instrumentation and applications of Raman spectroscopy," *Chem. Soc. Rev.* **45**(7), 1958–1979 (2016).
5. D. W. S. Shipp, F. S. Sinjab, and I. Notingher, "Raman spectroscopy: techniques and applications in the life sciences," *Adv. Opt. Photonics* **9**(2), 1–70 (2017).
6. A. Mahadevan-jansen and R. R. Richards-Kortum, "Raman spectroscopy for the detection of cancers and precancers," *J. Biomed. Opt.* **1**(1), 31–70 (1996).
7. M. Diem et al., "Applications of infrared and Raman microspectroscopy of cells and tissue in medical diagnostics: present status and future promises," *Spectrosc. An Int. J.* **27**(5–6), 463–496 (2012).
8. S. Wachsmann-Hogiu, T. Weeks, and T. Huser, "Chemical analysis in vivo and in vitro by Raman spectroscopy-from single cells to humans," *Curr. Opin. Biotechnol.* **20**(1), 63–73 (2009).
9. Q. Tu and C. Chang, "Diagnostic applications of Raman spectroscopy," *Biol. Med.* **8**, 545–558 (2012).
10. L. A. Austin, S. Osseiran, and C. L. Evans, "Raman technologies in cancer diagnostics," *Analyst* **141**(2), 476–503 (2016).
11. M. Jermyn et al., "A review of Raman spectroscopy advances with an emphasis on clinical translation challenges in oncology," *Phys. Med. Biol.* **61**, R370–R400 (2016).
12. J. Schleusener et al., "Perturbation factors in the clinical handling of a fiber-coupled Raman probe for cutaneous in vivo diagnostic Raman spectroscopy," *Appl. Spectrosc.* **69**(2), 243–256 (2015).
13. E. Cordero et al., "Evaluation of shifted excitation Raman difference spectroscopy and comparison to computational background correction methods applied to biochemical Raman spectra," *Sensors* **17**(8), 1724 (2017).
14. D. Wei, S. Chen, and Q. Liu, "Review of fluorescence suppression techniques in Raman spectroscopy," *Appl. Spectrosc. Rev.* **50**, 387–406 (2015).
15. T. Rojalin et al., "Fluorescence-suppressed time-resolved Raman spectroscopy of pharmaceuticals using complementary metal-oxide semiconductor (CMOS) single-photon avalanche diode (SPAD) detector," *Anal. Bioanal. Chem.* **408**(3), 761–774 (2016).
16. E. Canetta et al., "Modulated Raman spectroscopy for enhanced identification of bladder tumor cells in urine samples," *J. Biomed. Opt.* **16**(3), 037002 (2011).
17. M. T. Gebrekidan et al., "A shifted-excitation Raman difference spectroscopy (SERDS) evaluation strategy for the efficient isolation of Raman spectra from extreme fluorescence interference," *J. Raman Spectrosc.* **47**(2), 198–209 (2016).
18. K. Christian et al., "Raman difference spectroscopy: a non-invasive method for identification of oral squamous cell carcinoma," *Biomed. Opt. Express* **5**(9), 3252–3265 (2014).
19. R. Gautam et al., "Review of multidimensional data processing approaches for Raman and infrared spectroscopy," *EPJ Tech. Instrum.* **2**(1), 8 (2015).
20. T. W. Bocklitz et al., "A comprehensive study of classification methods for medical diagnosis," *J. Raman Spectrosc.* **40**(12), 1759–1765 (2009).
21. T. W. Bocklitz et al., "How to pre-process Raman spectra for reliable and stable models?," *Anal. Chim. Acta* **704**(1–2), 47–56 (2011).
22. C. Krafft et al., "Developments in spontaneous and coherent Raman scattering microscopic imaging for biomedical applications," *Chem. Soc. Rev.* **45**(7), 1819–1849 (2016).
23. E. M. Barroso et al., "Water concentration analysis by Raman spectroscopy to determine the location of the tumor border in oral cancer surgery," *Cancer Res.* **76**(20), 5945–5953 (2016).
24. I. P. Santos et al., "Implementation of a novel low-noise InGaAs detector enabling rapid near-infrared multichannel Raman spectroscopy of pigmented biological samples," *J. Raman Spectrosc.* **46**(7), 652–660 (2015).
25. D. Dussault and P. Hoess, "Noise performance comparison of ICCD with CCD and EMCCD cameras," *Proc. SPIE* **5563**, 195 (2004).
26. J. Zhao et al., "Integrated real-time Raman system for clinical in vivo skin analysis," *Ski. Res. Technol. Off. J. Int. Soc. Bioeng. Ski. [and] Int. Soc. Digit. Imaging Ski. [and] Int. Soc. Ski. Imaging* **14**(4), 484–492 (2008).
27. J. Qi, K. L. Bechtel, and W.-C. Shih, "Automated image curvature assessment and correction for high-throughput Raman spectroscopy and microscopy," *Biomed. Spectrosc. Imaging* **3**(4), 359–368 (2014).
28. Z. Huang et al., "Rapid near-infrared Raman spectroscopy system for real-time in vivo skin measurements," *Opt. Lett.* **26**(22), 1782–1784 (2001).
29. Y. Komachi et al., "Raman probe using a single hollow waveguide," *Opt. Lett.* **30**(21), 2942–2944 (2005).

30. S. O. Konorov et al., "Hollow-core photonic crystal fiber-optic probes for Raman spectroscopy," *Opt. Lett.* **31**(12), 1911–1913 (2006).

31. K. M. Tan et al., "Near-infrared Raman spectroscopy using hollow-core photonic bandgap fibers," *Opt. Commun.* **283**(16), 3204–3206 (2010).

32. S. Dochow et al., "Multicore fiber with integrated fiber Bragg gratings for background-free Raman sensing," *Opt. Express* **20**(18), 20156–20169 (2012).

33. I. Latka et al., "Fiber optic probes for linear and nonlinear Raman applications—current trends and future development," *Laser Photonics Rev.* **7**(5), 698–731 (2013).

34. U. Utzinger and R. R. Richards-Kortum, "Fiber optic probes for biomedical optical spectroscopy," *J. Biomed. Opt.* **8**(1), 121–147 (2003).

35. L. M. Almond et al., "Assessment of a custom-built Raman spectroscopic probe for diagnosis of early oesophageal neoplasia," *J. Biomed. Opt.* **17**(8), 081421 (2012).

36. J. C. C. Day et al., "A miniature confocal Raman probe for endoscopic use," *Phys. Med. Biol.* **54**(23), 7077–7087 (2009).

37. J. Mo et al., "High wavenumber Raman spectroscopy for in vivo detection of cervical dysplasia," *Anal. Chem* **81**(21), 8908–8915 (2009).

38. S. Duraipandian et al., "Simultaneous fingerprint and high-wavenumber confocal Raman spectroscopy enhances early detection of cervical precancer in vivo," *Anal. Chem.* **84**, 5913–5919 (2012).

39. S. Duraipandian et al., "In vivo diagnosis of cervical precancer using Raman spectroscopy and genetic algorithm techniques," *Analyst* **136**(20), 4328 (2011).

40. M. S. Bergholt, W. Zheng, and Z. Huang, "Characterizing variability in in vivo Raman spectroscopic properties of different anatomical sites of normal tissue in the oral cavity," *J. Raman Spectrosc.* **43**(2), 255–262 (2012).

41. J. Mo, W. Zheng, and Z. Huang, "Fiber-optic Raman probe couples ball lens for depth-selected Raman measurements of epithelial tissue," *Biomed. Opt. Express* **1**(1), 17–30 (2010).

42. J. Wang et al., "Development of a beveled fiber-optic confocal Raman probe for enhancing in vivo epithelial tissue Raman measurements at endoscopy," *Opt. Lett.* **38**(13), 2321–2323 (2013).

43. Z. Huang et al., "Integrated Raman spectroscopy and trimodal wide-field imaging techniques for real-time in vivo tissue Raman measurements at endoscopy," *Opt. Lett.* **34**(6), 758–760 (2009).

44. J. Wang et al., "Comparative study of the endoscope-based bevelled and volume fiber-optic Raman probes for optical diagnosis of gastric dysplasia in vivo at endoscopy," *Anal. Bioanal. Chem.* **407**(27), 8303–8310 (2015).

45. M. S. Bergholt et al., "Fiberoptic confocal Raman spectroscopy for real-time in vivo diagnosis of dysplasia in Barrett's esophagus," *Gastroenterology* **146**(1), 27–32 (2014).

46. S. Duraipandian et al., "Real-time Raman spectroscopy for in vivo, online gastric cancer diagnosis during clinical endoscopic examination," *J. Biomed. Opt.* **17**(8), 081418 (2012).

47. J. Wang et al., "Fiber-optic Raman spectroscopy for in vivo diagnosis of gastric dysplasia," *Faraday Discuss.* **187**, 377–392 (2016).

48. K. Lin et al., "Real-time in vivo diagnosis of nasopharyngeal carcinoma using rapid fiber-optic Raman spectroscopy," *Theranostics* **7**(14), 3517–3526 (2017).

49. J. T. Motz et al., "Real-time Raman system for in vivo disease diagnosis," *J. Biomed. Opt.* **10**(3), 031113 (2007).

50. J. T. Motz et al., "Optical fiber probe for biomedical Raman spectroscopy," *Appl. Opt.* **43**(3), 542–554 (2004).

51. A. S. Haka et al., "In vivo margin assessment during partial mastectomy breast surgery using Raman spectroscopy," *Cancer Res.* **66**(6), 3317–3322 (2006).

52. L. Lim et al., "Clinical study of noninvasive in vivo melanoma and nonmelanoma skin cancers using multimodal spectral diagnosis," *J Biomed. Opt.* **19**(11), 117003 (2014).

53. R. Shaikh et al., "In vivo Raman spectroscopy of human uterine cervix: exploring the utility of vagina as an internal control," *J. Biomed. Opt.* **19**(8), 087001 (2014).

54. A. Malik et al., "In vivo Raman spectroscopy-assisted early identification of potential second primary/recurrences in oral cancers: an exploratory study," *Head Neck* **39**(11), 2216–2223 (2017).

55. M. A. Short et al., "Development and preliminary results of an endoscopic Raman probe for potential in vivo diagnosis of lung cancers," *Opt. Lett.* **33**(7), 711–713 (2008).

56. H. C. McGregor et al., "Real-time endoscopic Raman spectroscopy for in vivo early lung cancer detection," *J. Biophotonics* **13**(1), 98–110 (2016).

57. M. A. Short et al., "Development and in vivo testing of a high frequency endoscopic Raman spectroscopy system for potential applications in the detection of early colonic neoplasia," *J. Biophotonics* **9**(1–2), 44–48 (2016).

58. M. Agenant et al., "Clinical superficial Raman probe aimed for epithelial tumor detection: phantom model results," *Biomed. Opt. Express* **5**(4), 1203 (2014).

59. R. O. P. Draga et al., "In vivo bladder cancer diagnosis by high-volume Raman spectroscopy," *Anal. Chem.* **82**(14), 5993–5999 (2010).

60. EmVision Advanced Optical Designs.

61. H. Ding et al., "In vivo analysis of mucosal lipids reveals histological disease activity in ulcerative colitis using endoscope-coupled Raman spectroscopy," *Biomed. Opt. Express* **8**(7), 3426–3439 (2017).

62. M. Jermyn et al., "Raman spectroscopy detects distant invasive brain cancer cells centimeters beyond MRI capability in humans," *Biomed. Opt. Express* **7**(12), 5129–5137 (2016).

63. J. Desroches et al., "Characterization of a Raman spectroscopy probe system for intraoperative brain tissue classification," *Biomed. Opt. Express* **6**(7), 2380 (2015).

64. M. Jermyn et al., "Intraoperative brain cancer detection with Raman spectroscopy in humans," *Sci. Transl. Med.* **7**(274), 274ra19 (2015).

65. C. M. O'Brien et al., "Characterization of human cervical remodeling throughout pregnancy using in vivo Raman spectroscopy," *J. Biomed. Opt.* **1**(1), 93032F (2015).

66. I. J. Pence et al., "Clinical characterization of in vivo inflammatory bowel disease with Raman spectroscopy," *Biomed. Opt. Express* **8**(2), 524–535 (2017).

67. J. Q. Nguyen et al., "Intraoperative Raman spectroscopy of soft tissue sarcomas," *Lasers Surg. Med.* **48**(8), 774–781 (2016).

68. H. Lui et al., "Real-time Raman spectroscopy for in vivo skin cancer diagnosis," *Cancer Res.* **72**(10), 2491–2500 (2012).

69. W. Wang et al., "Real-time in vivo cancer diagnosis using Raman spectroscopy: real-time in vivo cancer diagnosis using Raman spectroscopy," *J. Biophotonics* **8**(7), 527–545 (2015).

70. C. Fink and H. Haenssle, "Non-invasive tools for the diagnosis of cutaneous melanoma," *Ski. Res. Technol.* **23**(3), 261–271 (2017).

71. C. A. Lieber et al., "In vivo nonmelanoma skin cancer diagnosis using Raman microspectroscopy," *Lasers Surg. Med.* **40**(7), 461–467 (2008).

72. C. A. Lieber and A. Mahadevan-Jansen, "Development of a handheld Raman microspectrometer for clinical dermatologic applications," *Opt. Express* **15**(19), 11874–11882 (2007).

73. J. Schleusener et al., "In vivo study for the discrimination of cancerous and normal skin using fibre probe-based Raman spectroscopy," *Exp. Dermatol.* **24**(10), 767–772 (2015).

74. E. Y. M. Bonnist et al., "Understanding the dandruff scalp before and after treatment: an in vivo Raman spectroscopic study," *Int. J. Cosmet. Sci.* **36**(4), 347–354 (2014).

75. J. Lademann et al., "In vivo Raman spectroscopy detects increased epidermal antioxidative potential with topically applied carotenoids," *Laser Phys. Lett.* **6**(1), 76–79 (2009).

76. J. W. Fluhr et al., "Infant epidermal skin physiology: adaptation after birth," *Br. J. Dermatol.* **166**(3), 483–490 (2012).

77. C. Choe et al., "In vivo confocal Raman microscopic determination of depth profiles of the stratum corneum lipid organization influenced by application of various oils," *J. Dermatol. Sci.* **87**(2), 183–191 (2017).

78. M. B. Lopes et al., "In vivo confocal Raman spectroscopic analysis of the effects of infrared radiation in the human skin dermis," *Photochem. Photobiol.* **93**(2), 613–618 (2017).

79. C. Kendall et al., "Evaluation of Raman probe for oesophageal cancer diagnostics," *Analyst* **135**(12), 3038 (2010).

80. L. M. Almond et al., "Endoscopic Raman spectroscopy enables objective diagnosis of dysplasia in Barrett's esophagus," *Gastrointest. Endosc.* **79**(1), 37–45 (2014).

81. M. A. Short et al., "Using high frequency Raman spectra for colonic neoplasia detection," *Opt. Express* **21**(4), 5025–5034 (2013).

82. K. Lin, D. L. P. Cheng, and Z. Huang, "Optical diagnosis of laryngeal cancer using high wavenumber Raman spectroscopy," *Biosens. Bioelectron.* **35**(1), 213–217 (2012).

83. S. Koljenović et al., "Tissue characterization using high wave number Raman spectroscopy," *J. Biomed. Opt.* **10**(3), 031116 (2005).

84. P. Matousek et al., "Subsurface probing in diffusely scattering media using spatially offset Raman spectroscopy," *Appl. Spectrosc.* **59**(4), 393–400 (2005).

85. P. Matousek et al., "Numerical simulations of subsurface probing in diffusely scattering media using spatially offset Raman spectroscopy," *Appl. Spectrosc.* **59**(12), 1485–1492 (2005).

86. J. R. Maher and A. J. Berger, "Determination of ideal offset for spatially offset Raman spectroscopy," *Appl. Spectrosc.* **64**(1), 61–65 (2010).

87. "Spatially offset Raman spectroscopy (SORS)," Agilent.

88. P. Matousek et al., "Noninvasive Raman spectroscopy of human tissue in vivo," *Appl. Spectrosc.* **60**(7), 758–763 (2006).

89. K. Sowoidnich et al., "Spatially offset Raman spectroscopy for photon migration studies in bones with different mineralization levels," *Analyst* **142**(17), 3219–3226 (2017).

90. K. Buckley et al., "Towards the in vivo prediction of fragility fractures with Raman spectroscopy," *J. Raman Spectrosc.* **46**(7), 610–618 (2015).

91. K. Buckley et al., "Decomposition of in vivo spatially offset Raman spectroscopy data using multivariate analysis techniques," *J. Raman Spectrosc.* **45**(2), 188–192 (2014).

92. K. Buckley et al., "Measurement of abnormal bone composition in vivo using noninvasive Raman spectroscopy," *IBMS Bonekey* **11**, 602 (2014).

93. M. D. Keller, S. K. Majumder, and A. Mahadevan-Jansen, "Spatially offset Raman spectroscopy of layered soft tissues," *Opt. Lett.* **34**(7), 926–928 (2009).

94. M. D. Keller et al., "Development of a spatially offset Raman spectroscopy probe for breast tumor surgical margin evaluation," *J. Biomed. Opt.* **16**(7), 077006 (2011).

95. M. D. Keller et al., "Monte Carlo model of spatially offset Raman spectroscopy for breast tumor margin analysis," *Appl. Spectrosc.* **64**(6), 607–614 (2010).

96. G. Feng et al., "Sensitivity of spatially offset Raman spectroscopy (SORS) to subcortical bone tissue," *J. Biophotonics* **10**(8), 990–996 (2017).

97. S. V. K. Sekar et al., "Frequency offset Raman spectroscopy (FORS) for subsurface probing of diffusive medium," *Opt. Express* **25**, 889–896 (2017).

98. S. Konugolu Venkata Sekar et al., "Time domain diffuse Raman spectrometer based on novel TCSPC camera for depth analysis of diffusive media," *Opt. Lett.* **43**, 2134–2137 (2018).

99. C. A. Patil et al., "Combined Raman spectroscopy and optical coherence tomography device for tissue characterization," *Opt. Lett.* **33**(10), 1135–1137 (2008).

100. C. A. Patil et al., "Integrated system for combined Raman spectroscopy-spectral domain optical coherence tomography," *J. Biomed. Opt.* **16**(1), 011007 (2011).

101. C. A. Patil et al., "A clinical instrument for combined Raman spectroscopy-optical coherence tomography of skin cancers," *Lasers Surg. Med.* **2**, 143–151 (2011).

102. J. Wang et al., "Development of a hybrid Raman spectroscopy and optical coherence tomography technique for real-time in vivo tissue measurements," *Opt. Lett.* **41**(13), 3045–3048 (2016).

103. J. Wang et al., "Characterizing biochemical and morphological variations of clinically relevant anatomical locations of oral tissue in vivo with hybrid Raman spectroscopy and optical coherence tomography technique," *J. Biophotonics* **11**, e201700113 (2017).

104. M. Chen et al., "Depth-resolved multimodal imaging: wavelength modulated spatially offset Raman spectroscopy with optical coherence tomography," *J. Biophotonics* (2017).

105. A. C. De Luca et al., "Online fluorescence suppression in modulated Raman spectroscopy," *Anal. Chem.* **82**(2), 738–745 (2010).

106. M. Mazurenka et al., "Development of a combined OCT-Raman probe for the prospective in vivo clinical melanoma skin cancer screening," *Rev. Sci. Instrum.* **88**(10), 105103 (2017).

107. O. R. Šćepanović et al., "A multimodal spectroscopy system for real-time disease diagnosis," *Rev. Sci. Instrum.* **80**(4), 43103 (2009).

108. O. R. Šćepanović et al., "Multimodal spectroscopy detects features of vulnerable atherosclerotic plaque," *J. Biomed. Opt.* **16**(1), 011009 (2011).

109. M. Jermyn et al., "Highly accurate detection of cancer in situ with intraoperative, label-free, multimodal optical spectroscopy," *Cancer Res.* **77**(14), 1–10 (2017).

110. S. Dochow et al., "Combined fiber probe for fluorescence lifetime and Raman spectroscopy," *Anal. Bioanal. Chem.* **407**(27), 8291–8301 (2015).

111. M. Sharma et al., "Design and characterization of a novel multimodal fiber-optic probe and spectroscopy system for skin cancer applications," *Rev. Sci. Instrum.* **85**(8), 83101 (2014).

112. C. Matthäus et al., "Detection and characterization of early plaque formations by Raman probe spectroscopy and optical coherence tomography: an in vivo study on a rabbit model," *J. Biomed. Opt.* **23**(1), 015004 (2018).

113. L. A. Reisner et al., "A prototype biosensor-integrated image-guided surgery system," *Int. J. Med. Robot. Comput. Assist. Surg.* **3**(1), 82–88 (2007).

114. Araknes The BioRobotics Institute.

115. P. C. Ashok et al., "A Raman spectroscopy bio-sensor for tissue discrimination in surgical robotics," *J. Biophotonics* **7**(1–2), 103–109 (2014).

116. M. S. Bergholt et al., "In vivo, real-time, transnasal, image-guided Raman endoscopy: defining spectral properties in the nasopharynx and larynx," *J. Biomed. Opt.* **17**(7), 077002 (2012).

117. J. Schleusener et al., "Design and technical evaluation of fibre-coupled Raman probes for the image-guided discrimination of cancerous skin," *Meas. Sci. Technol.* **25**(3), 35701 (2014).

118. M. S. Bergholt et al., "Characterizing variability in in vivo Raman spectra of different anatomical locations in the upper gastrointestinal tract toward cancer detection," *J. Biomed. Opt.* **16**(3), 037003 (2011).

119. M. S. Bergholt et al., "In vivo diagnosis of gastric cancer using Raman endoscopy and ant colony optimization techniques," *Int. J. Cancer* **128**(11), 2673–2680 (2011).

120. M. S. Bergholt et al., "Fiber-optic Raman spectroscopy probes gastric carcinogenesis in vivo at endoscopy," *J. Biophotonics* **6**(1), 49–59 (2013).

121. M. S. Bergholt et al., "Combining near-infrared-excited autofluorescence and Raman spectroscopy improves in vivo diagnosis of gastric cancer," *Biosens. Bioelectron.* **26**(10), 4104–4110 (2011).

122. W. Wang et al., "Disposable sheath that facilitates endoscopic Raman spectroscopy," *J. Biomed. Opt.* **21**(2), 025001 (2016).

123. I. J. Pence, E. Vargis, and A. Mahadevan-Jansen, "Assessing variability of in vivo tissue Raman spectra," *Appl. Spectrosc.* **67**(7), 789–800 (2013).

124. J. Desroches et al., "Raman spectroscopy in microsurgery: impact of operating microscope illumination sources on data quality and tissue classification," *Analyst* **142**, 1185–1191 (2017).

125. P. I. Okagbare and M. D. Morris, "Polymer-capped fiber-optic Raman probe for non-invasive Raman spectroscopy," *Analyst* **137**(1), 77–81 (2012).

126. M. S. Bergholt et al., "Multivariate reference technique for quantitative analysis of fiber-optic tissue Raman spectroscopy," *Anal. Chem.* **85**(23), 11297–11303 (2013).

127. "WHO Global atlas on cardiovascular disease prevention and control," WHO.

128. P. R. Moreno, B. Marshik, and J. E. Muller, "Near-infrared s pectro-scopy," Chapter 16 in *The Vulnerable Atherosclerotic Plaque*, R. V. MD et al., Eds., pp. 257–262, Blackwell Publishing, Oxford, United Kingdom (2006).

129. M. Naghavi et al., "From vulnerable plaque to vulnerable patient: a call for new definitions and risk assessment strategies: part II," *Circulation* **108**(15), 1772–1778 (2003).

130. C. V. Bourantas et al., "Hybrid intravascular imaging: recent advances, technical considerations, and current applications in the study of plaque pathophysiology," *Eur. Heart J.* **38**(6), 400–412 (2017).

131. H. P. J. Buschman et al., "In vivo determination of the molecular composition of artery wall by intravascular Raman spectroscopy," *Anal. Chem.* **72**(16), 3771–3775 (2000).

132. J. T. Motz et al., "In vivo Raman spectral pathology of human atherosclerosis and vulnerable plaque," *J. Biomed. Opt.* **11**(2), 021003 (2006).

133. O. R. Šćepanović et al., "Detection of morphological markers of vulnerable atherosclerotic plaque using multimodal spectroscopy," *J. Biomed. Opt.* **11**(2), 021007 (2006).

134. C. Matthäus et al., "In vivo characterization of atherosclerotic plaque depositions by Raman-probe spectroscopy and in vitro coherent anti-stokes Raman scattering microscopic imaging on a rabbit model," *Anal Chem.* **84**(18), 7845–7851 (2012).

135. S. Dochow et al., "Comparing Raman and fluorescence lifetime spectroscopy from human atherosclerotic lesions using a bimodal probe," *J. Biophotonics* **9**(9), 958–966 (2016).

136. R. McQueenie et al., "Detection of inflammation in vivo by surface-enhanced Raman scattering provides higher sensitivity than conventional fluorescence imaging," *Anal. Chem.* **84**(14), 5968–5975 (2012).

137. A. Sahu et al., "Serum based diagnosis of asthma using Raman spectroscopy: an early phase pilot study," *PLoS One* **8**(11), e78921 (2013).

138. H. Nawaz et al., "Prediction of viral loads for diagnosis of hepatitis C infection in human plasma samples using Raman spectroscopy coupled with partial least squares regression analysis," *J. Raman Spectrosc.* **48**(5), 697–704 (2017).

139. G. E. Tontini et al., "Differential diagnosis in inflammatory bowel disease colitis: state of the art and future perspectives," *World J. Gastroenterol.* **21**(1), 21–46 (2015).

140. X. Bi et al., "Development of spectral markers for the discrimination of ulcerative colitis and Crohn's disease using Raman spectroscopy," *Dis. Colon Rectum* **54**(1), 48–53 (2011).

141. I. J. Pence et al., "Endoscopy-coupled Raman spectroscopy for in vivo discrimination of inflammatory bowel disease," *Proc. SPIE* **8939**, 89390R (2014).

142. B. Krishnapuram et al., "Sparse multinomial logistic regression: fast algorithms and generalization bounds," *IEEE Trans. Pattern Anal. Mach. Intell.* **27**(6), 957–968 (2005).

143. R. L. Siegel, K. D. Miller, and A. Jemal, "Cancer statistics, 2017," *CA. Cancer J. Clin.* **67**(1), 7–30 (2017).

144. F. Islami, L. A. Torre, and A. Jemal, "Global trends of lung cancer mortality and smoking prevalence," *Transl. Lung Cancer Res.* **4**(4), 327–338 (2015).

145. "Screening by chest radiograph and lung cancer mortality: the prostate, lung, colorectal, and ovarian (PLCO) randomized trial," *JAMA* **306**(17), 1865–1873 (2011).

146. D. Sharma, T. G. Newman, and W. S. Aronow, "Lung cancer screening: history, current perspectives, and future directions," *Arch. Med. Sci. AMS* **11**(5), 1033–1043 (2015).

147. P. Zarogoulidis, K. Zarogoulidis, and K. Tsakiridis, "Lung cancer: an update on current and future diagnostic and treatment techniques," *J. Thorac. Dis.* **5**(4), S341 (2013).

148. N. Ikeda et al., "Comprehensive diagnostic bronchoscopy of central type early stage lung cancer," *Lung Cancer* **56**(3), 295–302 (2007).

149. M. Andolfi et al., "The role of bronchoscopy in the diagnosis of early lung cancer: a review," *J. Thoracic Dis.* **8**(11), 3329–3337 (2016).

150. J. Sun et al., "The value of autofluorescence bronchoscopy combined with white light bronchoscopy compared with white light alone in the diagnosis of intraepithelial neoplasia and invasive lung cancer: a meta-analysis," *J. Thorac. Oncol.* **6**(8), 1336–1344 (2011).

151. N. D. Magee et al., "Ex vivo diagnosis of lung cancer using a Raman miniprobe," *J. Phys. Chem. B* **113**(23), 8137–8141 (2009).

152. H. Zeng et al., "In vivo Raman spectroscopy for early lung cancer detection," *Cancer Res.* **2**, 7112 (2011).

153. H. C. McGregor et al., "In vivo real-time endoscopic Raman spectroscopy for improving early lung cancer detection," in *Asia Communications and Photonics Conf. (2015)* (2015).

154. M. Ghoncheh, Z. Pournamdar, and H. Salehiniya, "Incidence and mortality and epidemiology of breast cancer in the World," *Asian Pacific J. Cancer Prev.* **17**(Suppl. 3), 43–46 (2016).

155. D. Roganovic et al., "Breast MRI, digital mammography and breast tomosynthesis: comparison of three methods for early detection of breast cancer," *Bosn. J. Basic Med. Sci.* **15**(4), 64–68 (2015).

156. A. L. Siu, "Screening for Breast Cancer: U.S. preventive services task force recommendation statement," *Ann. Intern. Med.* **164**(4), 279 (2016).

157. B. Brożek-Płuska et al., "Breast cancer diagnostics by Raman spectroscopy," *J. Mol. Liq.* **141**(3), 145–148 (2008).

158. H. Abramczyk et al., "The label-free Raman imaging of human breast cancer," *J. Mol. Liq.* **164**(1–2), 123–131 (2011).

159. H. Abramczyk et al., "Raman 'optical biopsy' of human breast cancer," *Prog. Biophys. Mol. Biol.* **108**(1–2), 74–81 (2012).

160. A. Saha et al., "Raman spectroscopy: a real-time tool for identifying microcalcifications during stereotactic breast core needle biopsies," *Biomed. Opt. Express* **2**(10), 2792 (2011).

161. K. E. Shafer-Peltier et al., "Raman microspectroscopic model of human breast tissue: implications for breast cancer diagnosis in vivo," *J. Raman Spectrosc.* **33**(7), 552–563 (2002).

162. J. Horsnell, "The use of Raman spectroscopy for the intra-operative assessment of axillary lymph nodes in breast cancer," PhD Thesis, Cranfield University (2012).

163. A. S. Haka et al., "Diagnosing breast cancer using Raman spectroscopy: prospective analysis," *J. Biomed. Opt.* **14**(5), 054023 (2009).

164. Q. Li, Q. Gao, and G. Zhang, "Classification for breast cancer diagnosis with Raman spectroscopy," *Biomed. Opt. Express* **5**(7), 2435 (2014).

165. F. Bray et al., "Global estimates of cancer prevalence for 27 sites in the adult population in 2008," *Int. J. Cancer* **132**(5), 1133–1145 (2013).

166. D. Forman et al., *Cancer Incidence in Five Continents*, Vol. X, IARC Scientific Publication No. 164 (2014).

167. G. K. Malhotra et al., "Global trends in esophageal cancer," *J. Surg. Oncol.* **115**(5), 564–579 (2017).

168. S. K. Teh et al., "Diagnosis of gastric cancer using near-infrared Raman spectroscopy and classification and regression tree techniques," *J. Biomed. Opt.* **13**(3), 034013 (2008).

169. Z. Huang et al., "In vivo early diagnosis of gastric dysplasia using narrow-band image-guided Raman endoscopy," *J. Biomed. Opt.* **15**(3), 037017 (2010).

170. S. K. Teh et al., "Near-infrared Raman spectroscopy for early diagnosis and typing of adenocarcinoma in the stomach," *Br. J. Surg.* **97**(4), 550–557 (2010).

171. J. Wang et al., "Simultaneous fingerprint and high-wavenumber fiber-optic Raman spectroscopy improves in vivo diagnosis of esophageal squamous cell carcinoma at endoscopy," *Sci. Rep.* **5**(1), 12957 (2015).

172. K. Lin et al., "Rapid fiber-optic Raman spectroscopy for real-time in vivo detection of gastric intestinal metaplasia during clinical gastroscopy," *Cancer Prev. Res.* **9**(6), 476–483 (2016).

173. S. K. Teh et al., "Diagnostic potential of near-infrared Raman spectroscopy in the stomach: differentiating dysplasia from normal tissue," *Br. J. Cancer* **98**(2), 457–465 (2008).

174. Z. Huang et al., "In vivo detection of epithelial neoplasia in the stomach using image-guided Raman endoscopy," *Biosens. Bioelectron.* **26**(2), 383–389 (2010).

175. M. S. Bergholt et al., "Raman endoscopy for in vivo differentiation between benign and malignant ulcers in the stomach," *Analyst* **135**(12), 3162 (2010).

176. S. K. Teh et al., "Spectroscopic diagnosis of laryngeal carcinoma using near-infrared Raman spectroscopy and random recursive partitioning ensemble techniques," *Analyst* **134**(6), 1232–1239 (2009).

177. G. Shetty et al., "Raman spectroscopy: elucidation of biochemical changes in carcinogenesis of oesophagus," *Br. J. Cancer* **94**(10), 1460–1464 (2006).

178. A. May et al., "Accuracy of staging in early oesophageal cancer using high resolution endoscopy and high resolution endosonography: a comparative, prospective, and blinded trial," *Gut* **53**(5), 634–640 (2004).

179. M. S. Bergholt et al., "Real-time depth-resolved fiber optic Raman endoscopy for in vivo diagnosis of gastric precancer," *Proc. SPIE* **8939**, 89390M (2014).

180. M. S. Bergholt et al., "Characterizing variability of in vivo Raman spectroscopic properties of different anatomical sites of normal colorectal tissue towards cancer diagnosis at colonoscopy," *Anal. Chem.* **87**(2), 960–966 (2015).

181. H. Ding et al., "Effect of physiological factors on the biochemical properties of colon tissue—an in vivo Raman spectroscopy study: physiological factors on the biochemical properties of colon tissue," *J. Raman Spectrosc.* **48**(7), 902–909 (2017).

182. S. Antoni et al., "Bladder cancer incidence and mortality: a global overview and recent trends," *in Eur. Urol.* **71**(1), 96–108 (2017).

183. B. W. D. De Jong et al., "Raman spectroscopic detection of changes in molecular composition of bladder muscle tissue caused by outlet obstruction," *Vib. Spectrosc.* **32**(1), 57–65 (2003).

184. B. W. D. De Jong et al., "Discrimination between nontumor bladder tissue and tumor by Raman spectroscopy," *Anal. Chem.* **78**(22), 7761–7769 (2006).

185. I. Barman et al., "Selective sampling using confocal Raman spectroscopy provides enhanced specificity for urinary bladder cancer diagnosis," *Anal. Bioanal. Chem.* **404**(10), 3091–3099 (2012).

186. M. C. M. Grimbergen et al., "Bladder cancer diagnosis during cystoscopy using Raman spectroscopy," *Proc. SPIE* **7161**, 716114 (2009).

187. N. Stone et al., "The use of Raman spectroscopy to provide an estimation of the gross biochemistry associated with urological pathologies," *Anal. Bioanal. Chem.* **387**(5), 1657–1668 (2007).

188. P. Crow et al., "Assessment of fiberoptic near-infrared Raman spectroscopy for diagnosis of bladder and prostate cancer," *Urology* **65**(6), 1126–1130 (2005).

189. C. R. Leemans, B. J. M. Braakhuis, and R. H. Brakenhoff, "The molecular biology of head and neck cancer," *Nat. Rev. Cancer* **11**(1), 9 (2011).

190. G. Carioli et al., "Global trends in nasopharyngeal cancer mortality since 1970 and predictions for 2020: focus on low-risk areas," *Int. J. Cancer* **140**(10), 2256–2264 (2017).

191. D. P. Lau et al., "Raman spectroscopy for optical diagnosis in the larynx: preliminary findings," *Lasers Surg. Med.* **37**(3), 192–200 (2005).

192. H. Chang et al., "Light-induced autofluorescence spectroscopy for detection of nasopharyngeal carcinoma in vivo," *Appl. Spectrosc.* **56**(10), 1361–1367 (2002).

193. L. T. Perelman, "Optical diagnostic technology based on light scattering spectroscopy for early cancer detection," *Expert Rev. Med. Dev.* **3**(6), 787–803 (2006).

194. D. P. Lau et al., "Raman spectroscopy for optical diagnosis in normal and cancerous tissue of the nasopharynx—preliminary findings," *Lasers Surg. Med.* **32**(3), 210–214 (2003).

195. S. Devpura et al., "Diagnosis of head and neck squamous cell carcinoma using Raman spectroscopy: tongue tissues," *J. Raman Spectrosc.* **43**(4), 490–496 (2012).

196. E. M. Barroso et al., "Discrimination between oral cancer and healthy tissue based on water content determined by Raman spectroscopy," *Anal. Chem.* **87**(4), 2419–2426 (2015).

197. H. Krishna et al., "Anatomical variability of in vivo Raman spectra of normal oral cavity and its effect on oral tissue classification," *Biomed. Spectrosc. Imaging* **2**(3), 199–217 (2013).

198. K. Lin et al., "Real-time in vivo diagnosis of laryngeal carcinoma with rapid fiber-optic Raman spectroscopy," *Biomed. Opt. Express* **7**(9), 3705–3715 (2016).

199. Z. Huang et al., "Raman spectroscopy in combination with background near-infrared autofluorescence enhances the in vivo assessment of malignant tissues," *Photochem. Photobiol.* **81**(5), 1219–1226 (2005).

200. G. A. Alexiou et al., "Management of meningiomas," *Clin. Neurol. Neurosurg.* **112**(3), 177–182 (2010).

201. O. Schillaci et al., "Single-photon emission computed tomography/computed tomography in brain tumors," *Semin. Nucl. Med.* **37**(1), 34–47 (2007).

202. S. M. K. Belhawi et al., "Early postoperative MRI overestimates residual tumour after resection of gliomas with no or minimal enhancement," *Eur. Radiol.* **21**(7), 1526–1534 (2011).

203. T. W. Vitaz, "Techniques to improve the extent of brain tumor resection—awake speech and motor mapping, and intraoperative MRI," in *Molecular Considerations and Evolving Surgical Management Issues in the Treatment of Patients with a Brain Tumor*, T. Lichtor, Ed., IntechOpen Limited, London, United Kingdom (2015).

204. T. B. Belsuzarri, R. A. Sangenis, and J. M. Araujo, "Brain tumor surgery: supplemental intra-operative imaging techniques and future challenges," *J. Cancer Metastasis Treat.* **2**, 70–79 (2016).

205. M. Kirsch et al., "Raman spectroscopic imaging for in vivo detection of cerebral brain metastases," *Anal. Bioanal. Chem.* **398**(4), 1707–1713 (2010).

206. J. Zhang et al., "Accuracy of Raman spectroscopy in differentiating brain tumor from normal brain tissue," *Oncotarget* **8**(22), 36824–36831 (2017).

207. D. G. Leslie et al., "Identification of pediatric brain neoplasms using Raman spectroscopy," *Pediatr. Neurosurg.* **48**(2), 109–117 (2012).

208. F. Leblond et al., "Intraoperative detection of cancerous brain tissue using Raman spectroscopy," *SPIE Newsroom* 4–6 (2015).

209. A. Beljebbar et al., "Ex vivo and in vivo diagnosis of C6 glioblastoma development by Raman spectroscopy coupled to a microprobe," *Anal. Bioanal. Chem.* **398**(1), 477–487 (2010).

210. T. Liu et al., "Evaluation of Raman spectra of human brain tumor tissue using the learning vector quantization neural network," *Laser Phys.* **26**(5), 55606 (2016).

211. S.-L. Chen et al., "Prostate cancer mortality-to-incidence ratios are associated with cancer care disparities in 35 countries," *Sci. Rep.* **7**, 40003 (2017).

212. GLOBOCAN cancer fact sheets: cervical cancer.

213. L. Rotter et al., "Dysplasia and cervical cancer: current diagnostic possibilities," *Ces. Gynekol.* **79**(4), 314–320 (2014).

214. A. J. Blatt et al., "Comparison of cervical cancer screening results among 256, 648 women in multiple clinical practices," *Cancer Cytopathol.* **123**(5), 282–288 (2015).

215. R. S. DaCosta, B. C. Wilson, and N. E. Marcon, "Fluorescence and spectral imaging," *Sci. World J.* **7**, 2046–2071 (2007).

216. Y. N. Mirabal et al., "Reflectance spectroscopy for in vivo detection of cervical precancer," *J. Biomed. Opt.* **7**(4), 587–594 (2002).

217. S. Duraipandian et al., "Integrated fingerprint and high wavenumber confocal Raman spectroscopy for in vivo diagnosis of cervical precancer," *Proc. SPIE* **8572**, 85720Z (2013).

218. A. Robichaux-Viehoever et al., "Characterization of Raman spectra measured in vivo for the detection of cervical dysplasia," *Appl. Spectrosc.* **61**(9), 986–993 (2007).

219. J. T. Marquês et al., "Biomembrane organization and function: the decisive role of ordered lipid domains," in *Advances in Planar Lipid Bilayers and Liposomes* Vol. 22, A. Iglič, C. V. Kulkarni, and M. Rappolt, Eds., pp. 65–96, Academic Press, London, United Kingdom (2015).

220. E. Vargis et al., "Sensitivity of Raman spectroscopy to normal patient variability," *J. Biomed. Opt.* **16**(11), 117004 (2011).

221. S. Duraipandian et al., "Effect of hormonal variation on in vivo high wavenumber Raman spectra improves cervical precancer detection," *Proc. SPIE* **8214**, 82140A (2012).

222. S. Duraipandian et al., "Near-infrared-excited confocal Raman spectroscopy advances in vivo diagnosis of cervical precancer," *J. Biomed. Opt.* **18**(6), 067007 (2013).

223. S. Duraipandian et al., "Near-infrared Raman spectroscopy for assessing biochemical changes of cervical tissue associated with precarcinogenic transformation," *Analyst* **139**(21), 5379–5386 (2014).

224. P. Crow et al., "The use of Raman spectroscopy to identify and grade prostatic adenocarcinoma in vitro," *Br. J. Cancer* **89**(1), 106 (2003).

225. S. Devpura et al., "Detection of benign epithelia, prostatic intraepithelial neoplasia, and cancer regions in radical prostatectomy tissues using Raman spectroscopy," *Vib. Spectrosc.* **53**(2), 227–232 (2010).

226. N. Kourkoumelis et al., "Advances in the in vivo Raman spectroscopy of malignant skin tumors using portable instrumentation," *Int. J. Mol. Sci.* **16**(7), 14554–14570 (2015).

227. J. Zhao et al., "Using Raman spectroscopy to detect and diagnose skin cancer in vivo," *Dermatol. Clin.* **35**, 495–504 (2017).

228. G. Monheit et al., "The performance of MelaFind: a prospective multicenter study," *Arch. Dermatol.* **147**(2), 188–194 (2010).

229. X. Feng et al., "Raman active components of skin cancer," *Biomed. Opt. Express.* **8**(6), 2835–2850 (2017).

230. M. Jermyn et al., "Neural networks improve brain cancer detection with Raman spectroscopy in the presence of light artifacts," *Proc. SPIE* **9690**, 96900B (2016).

Eliana Cordero obtained her BSc degree in mechatronic engineering from the University of Pamplona in 2011 and her MSc degree in scientific instrumentation from Ernst Abbe University of Applied Science of Jena. She enrolled PhD studies at the faculty for chemistry and earth sciences, Friedrich Schiller University of Jena in 2016. Since there, she is employed at the Leibniz institute of Photonic Technology, where she works in the development of Raman probes for endoscopic applications.

Ines Latka studied physics at the Technical University Ilmenau and the Friedrich–Schiller University Jena. After her diploma thesis she worked several years on the field of fiber optic sensors, particularly with fiber Bragg gratings. In 2009, she joined the molecular imaging group at IPHT in Jena/Germany, focusing on CARS. Her current

interests are focused on the development of fiber optic endoscopes for medical applications, e.g., employing Raman spectroscopy, in conjunction with multimodal instrumentation.

Christian Matthäus is working as a research assistant at Leibniz Institute for Photonic Technology (IPHT), Jena, Germany. His current interests are Raman spectroscopy, nonlinear imaging techniques, and MALDI-TOF. He received his PhD from City University of New York in 2006 in the field of spectroscopic imaging. After a postdoc position at Northeastern University, Boston, he joined the group of Prof. Jürgen Popp at the IPHT in 2009.

Iwan W. Schie studied medical engineering at Beuth University of Applied Science, Berlin, and received his PhD in biomedical engineering from the University of California, Davis. During his PhD his research focus was on instrument development and medical applications for multiphoton microscopy and spontaneous Raman spectroscopy. Since 2014, he has been working as a postdoctoral researcher at the Leibniz-IPHT and established the group for "Multimodal Instrumentation" at the Leibniz-IPHT in 2017, with the research focus on high-throughput Raman spectroscopy systems for single cell classification, fiber-probe development, and instrumentation for medical in-vivo applications.

Jürgen Popp studied chemistry at the universities of Erlangen and Würzburg. After his PhD in chemistry he joined Yale University for postdoctoral work. He subsequently returned to Würzburg University where he finished his habilitation in 2002. Since 2002, he has held a chair for Physical Chemistry at the Friedrich–Schiller University Jena. Since 2006, he is also the scientific director of the Leibniz Institute of Photonic Technology, Jena. His research interests are mainly concerned with biophotonics. In particular his expertise in the development and application of innovative Raman techniques for biomedical diagnosis should be emphasized.